

Visiting Scientist mission report


Document NWPSAF-KN-VS-012

Version 1.0

26 March 2013

Second-order structure function analysis of scatterometer winds over the tropical Pacific: Part 2. Rainy and dry regions

Gregory P. King, Jur Vogelzang and Ad Stoffelen

<p>The EUMETSAT Network of Satellite Application Facilities</p>	 <p>NWP SAF Numerical Weather Prediction</p>	<p>Second-order structure function analysis of scatterometer winds over the tropical Pacific: Part 2. Rainy and dry regions</p>	<p>Doc ID : NWPSAF-KN-VS-012 Version : 1.0 Date : 26.3.13</p>
---	--	---	---

This documentation was developed within the context of the EUMETSAT Satellite Application Facility on Numerical Weather Prediction (NWP SAF), under the Cooperation Agreement dated 29 June 2011, between EUMETSAT and the Met Office, UK, by one or more partners within the NWP SAF. The partners in the NWP SAF are the Met Office, ECMWF, KNMI and Météo France.

Copyright 2013, EUMETSAT, All Rights Reserved.

Change record			
Version	Date	Author / changed by	Remarks
1.0	26.3.13	G.P.King, J.Vogelzang and A.Stoffelen	Final version for publication on NWP SAF website

Second-order structure function analysis of scatterometer winds over the Tropical Pacific: Part 2. Rainy and dry regions

Gregory P. King^{1,2}, Jur Vogelzang³ and Ad Stoffelen³

¹Centro de Geofísica - IDL, Campo Grande, C8, University of Lisbon, 1749-016, Lisbon, Portugal

²Instituto Gulbenkian de Ciência, Apartado 14, 2781-901 Oeiras, Portugal

³KNMI Royal Netherlands Meteorological Institute, Postbus 201, 3730 AE De Bilt, The Netherlands

Abstract

Kolmogorov second-order structure functions (second moment of velocity differences) are used to characterize and compare the small scale information contained in five scatterometer wind products: three were derived from the SeaWinds-on-QuikSCAT scatterometer and two from the ASCAT-on-MetOp-A scatterometer. An important difference in these products is the method used to remove ambiguities. A median filter method was used to produce two of the SeaWinds products, while a variational method (known as 2DVAR) was used to produce both ASCAT and one of the SeaWinds products. The analysis is carried out for rainy and dry regions in the tropical Pacific (nine regions between latitudes 10°S and 10°N and longitudes 140° and 260°E) for the period November 2008 – October 2009. Both longitudinal and transverse structure functions, calculated using separations in the along-track (meridional) direction, are calculated from monthly and regionally averaged velocity differences. Structure functions were characterized by estimating noise levels (the extrapolated value at zero separation), turbulent kinetic energy (structure function magnitude at 300 km), and structure function slope from fits in log-log space over the range 50 – 250 km.

The five wind products show good qualitative agreement, but instrument and processing differences reveal important differences. Estimates of noise level are sensitive to the method used. Fits to a symmetric quadratic yield noise levels that correlate well with rain-rate. These noise levels also show that SeaWinds median filter products have larger noise in the transverse component, while ASCAT products have larger noise in the longitudinal component. Fits to an asymmetric quadratic yields information about the strength of the filtering used to reduce noise

in Level 1 processing; results imply that ASCAT products are over filtered. Estimates of the turbulent kinetic energy show that ASCAT is greater than (less than) or equal to SeaWinds in the divergent (shear) component. Ratios of the shear to divergent turbulent kinetic energy shows that the greatest differences between SeaWinds median filtered and ASCAT winds occur in the convectively active months of each region. Longitudinal (transverse) structure function slopes are steeper (shallower) for SeaWinds than for ASCAT. Slope ratios in most regions show that SeaWinds median filtered winds have steeper longitudinal structure functions, while ASCAT has steeper transverse structure functions. Results for the SeaWinds 2DVAR winds vary, sometimes closer to ASCAT and sometimes closer to the other SeaWinds products.

Contents

1	Introduction	6
2	Physical context	7
3	Scatterometers and data description	9
3.1	Data	11
3.1.1	Wind data	11
3.1.2	NWP data	12
3.1.3	Rain data	12
3.1.4	Ambiguity removal and noise	12
3.2	Study areas	13
3.3	Samples	16
4	Data Analysis	16
4.1	Second-order structure functions	16
4.1.1	Definitions	16
4.1.2	Theoretical relationships for 2D turbulence	17
4.1.3	Relationship with velocity covariance function	17
4.1.4	Relationship with spectra	18
4.2	Application to scatterometer winds	18
5	Structure functions and their characteristics	19
6	Noise Levels	20

7	A proxy for the turbulent kinetic energy	30
8	Structure Function Slopes	34
9	A note on OMB structure functions	38
10	Summary	47

List of Tables

1	Orbital parameters. The Equator Crossing Time is the local solar time of the satellite's passage over the equator.	9
2	ASCAT and SeaWinds products.	10
3	Geographical limits and nomenclature for the regions shown in Fig. 3. . .	13
4	Ranking of noise levels from largest (1) to smallest (5). The ranking of the SeaWinds-KNMI SQ-T noise level is sometimes larger and sometimes smaller than ASCAT noise levels. SQ levels were always greater than zero, while ASQ levels were either positive or negative (as indicated in parentheses).	21

List of Figures

1	SST field and superimposed ocean wind vectors for a typical January in the Tropical Pacific. Labels identify the Inter-Tropical and South Pacific Convergence Zones (ITCZ and SPCZ).	8
2	Latitude-time plots of monthly and zonally averaged SST measured by the TRMM Microwave Imager (TMI) during the study period.	8
3	The boundaries of the nine geographical regions used in the present study. Nomenclature of the regions and their geographical limits are given in Table 3.	13
4	Latitude-time plots of monthly and zonally averaged rain-rate measured by the TRMM Microwave Imager (TMI) during the study period.	15
5	Box and monthly-averaged SRad rain-rates.	15
6	Structure functions for the equatorial regions (a) Longitudinal and (b) Transverse; West Pacific (left) and East Pacific (right). The vertical lines are drawn at 50 and 250 km.	23
7	Same as Fig. 6, but for August 2009.	24
8	D_{TTa}/D_{LLa} vs. separation r in the Equatorial regions. Top: January 2009; Bottom: August 2009.	25
9	SQ-L noise levels (from fits to a symmetric quadratic fit) and SRad rain-rates (bars)	25
10	SQ-T noise levels and SRad rain-rates (bars).	26
11	SQ noise level ratios (T/L).	27

12	ASQ-L noise levels (from fits to an asymmetric quadratic) and SRad rain-rates (bars).	28
13	ASQ-T noise levels and SRad rain-rates (bars).	29
14	Mesoscale turbulent kinetic energy K_{La} as a function of month and wind product. The color coding is the same as used in Fig. 6.	31
15	As in Fig. 14, but for K_{Ta}	32
16	The monthly variability of vorticity-to-divergence as measured by the ratio K_{Ta}/K_{La}	33
17	Monthly variability of β_L and dependence on wind product.	35
18	Monthly variability of β_T and dependence on wind product.	36
19	Slope ratios β_T/β_L	37
20	D_{LL}^{omb} for ASCAT-12.5, January 2009	39
21	D_{TT}^{omb} for ASCAT-12.5, January 2009	40
22	D_{LL}^{omb} for ASCAT-12.5, August 2009	41
23	D_{TT}^{omb} for ASCAT-12.5, August 2009	42
24	D_{LL}^{omb} vs r for QSCAT-12.5, January 2009	43
25	D_{TT}^{omb} vs r for QSCAT-12.5, January 2009	44
26	D_{LL}^{omb} vs r for QSCAT-12.5, August 2009	45
27	D_{TT}^{omb} vs r for QSCAT-12.5, August 2009	46

1 Introduction

The ocean and atmosphere exchange heat, moisture and momentum across the air/sea boundary through interactions with small-scale structures in the near-surface winds. This exchange affects atmosphere and ocean circulations, weather and climate. In order to improve their modelling and prediction, measurement of near-surface ocean winds at high resolution over the global oceans is required. This can only be done using scatterometers carried on orbiting satellites.

Satellite scatterometers transmit microwaves towards the Earth and measure the back-scattered radiation from the wind-roughened ocean surface. Sophisticated processing results in high quality ocean vector winds that resolve small-scale (i.e., < 1000 km) structure in the near-surface ocean wind field. Forecasters use satellite winds in marine weather prediction, wave and surge forecasting, and the monitoring of tropical cyclones and prediction of their trajectories. They are used in numerical weather prediction (NWP), for driving ocean models, and to investigate climate variability in both the atmosphere and the ocean (*Bourassa et al., 2010*). Investigations of climate variability require long and consistent time series, which requires that the surface winds measured by different scatterometers be “patched” together. If not identified and corrected, errors and inconsistencies in the winds derived from different scatterometers will build up over time, leading to erroneous conclusions.

Small-scale structure can be efficiently described using statistical methods developed in the theory of isotropic turbulence: namely, spatial wavenumber spectra and structure functions (correlation functions of velocity differences). Spectral analysis has been used to make comparisons with two-dimensional turbulence theories (*Freilich and Chelton, 1986; Wikle et al., 1999; Patoux and Brown, 2001; Xu et al., 2011*), and to compare the effects of noise and processing on the effective resolution of winds derived from the Advanced Scatterometer (ASCAT) onboard the MetOp-A satellite and the SeaWinds scatterometer onboard the QuikSCAT satellite (*Vogelzang et al., 2011*). However, spectral analysis has limitations. It cannot be applied if samples have too many missing points. Missing points arise from instrument outage or because the retrieved wind is of low-quality. Low quality wind-retrievals are mainly due to radar contamination caused by rain, land or ice. Another limitation is that, due to the Fast Fourier Transform algorithm, samples need to be rather long (say, 128 points or more), making it difficult to investigate small regions with particular turbulence characteristics. The structure function calculation avoids these limitations.

The objective of this paper is to characterize and compare the small scale structure in the near-surface winds over the tropical Pacific derived from the ASCAT and SeaWinds scatterometers. The tropical Pacific contains both rainy and dry regions: heavy rain over warm pools and in convergence zones, and little or no rain over the cold tongue. As a result, a spectral analysis of the winds in this heterogeneous and climatically important region is difficult, as was demonstrated in an earlier report (*King et al., 2012*). Therefore we calculate structure functions. Monthly and regional averages are presented for the period November 2008 – October 2009 (the last 12 months of the QuikSCAT mission when both scatterometers were collecting winds).

The paper is organized as follows. Section 2 places our study in context with a brief description of the main convergence zones, the cold tongue and their seasonality. Section 3 describes the ASCAT and SeaWinds scatterometers, lists and briefly describes the wind products and their processing. The subdivision of the tropics into rainy and dry subregions, justified using rain-rates measured by the Tropical Rain Measuring Mission and the SeaWinds radiometer (SRad), is also given in this section. Section 4 contains the basic definitions and formulas for the second-order structure function and its relationship to the autocorrelation function and the spectrum. Theoretical relationships derived for homogeneous isotropic two-dimensional turbulence are summarized. These are used in later sections to help guide the analysis and interpret the results.

The main results are presented in sections 5–8. Section 5 presents structure functions for the west and east Pacific to illustrate their variability as a function of scale, region, time of year, and wind product. We identify three quantities that are then used to compare structure functions: noise level, slope and amplitude. Noise levels are useful as an indicator of wind product quality. Structure functions are by definition zero at zero separation ($r = 0$). However, real measurements are contaminated by noise, and, in the case of white noise, this gives rise to a spike at $r = 0$. In section 6, two methods are used to estimate the noise level. The results are sensitive to the method: one correlates with rain-rates, while the other reflects the spatial filtering used to reduce noise. The small scale structures missed by NWP but resolved by scatterometer measurements can be characterized in terms of the turbulent kinetic energy contained in those scales and its scaling. The structure function amplitude at scale r is used as a proxy for the turbulent kinetic energy. The regional and monthly variability of the structure function amplitude and slope, and how they vary with wind product, is presented in sections 7 and 8. In section 9 some structure functions for the observations - background (OMB) wind field are presented. OMB structure functions could find use in data assimilation. A summary of the results is given in section 10.

2 Physical context

Figure 1 shows sea surface temperatures (SST) for a typical August in the tropical Pacific between latitudes 30°S and 30°N; ocean wind vectors are superimposed on the SST in the figure. The convergence zones labeled in the figure play a central role in the organization of tropical circulations and generation of tropical weather systems. They are the InterTropical Convergence Zone (ITCZ), the western North Pacific Monsoon Trough (MT), the South Pacific Convergence Zone (SPCZ), and the East Pacific Warm Pool (EPWP). Also shown (Figure 2) are latitude-time plots of the monthly averaged SST over the period November 2008 - October 2009 in each longitudinal zone of the study area (see Fig. 3).

The ITCZ extends across the Pacific but in the east Pacific remains north of 4°N throughout the year. As boreal summer progresses, the ITCZ migrates north, merging with the EPWP in the eastern Pacific and with the MT in the western Pacific. The axis of the MT usually emerges from east Asia in boreal summer at about 20°- 25° N and extends south-eastward to a terminus southeast of Guam at (13° N, 145° E). Its oceanic portion shows

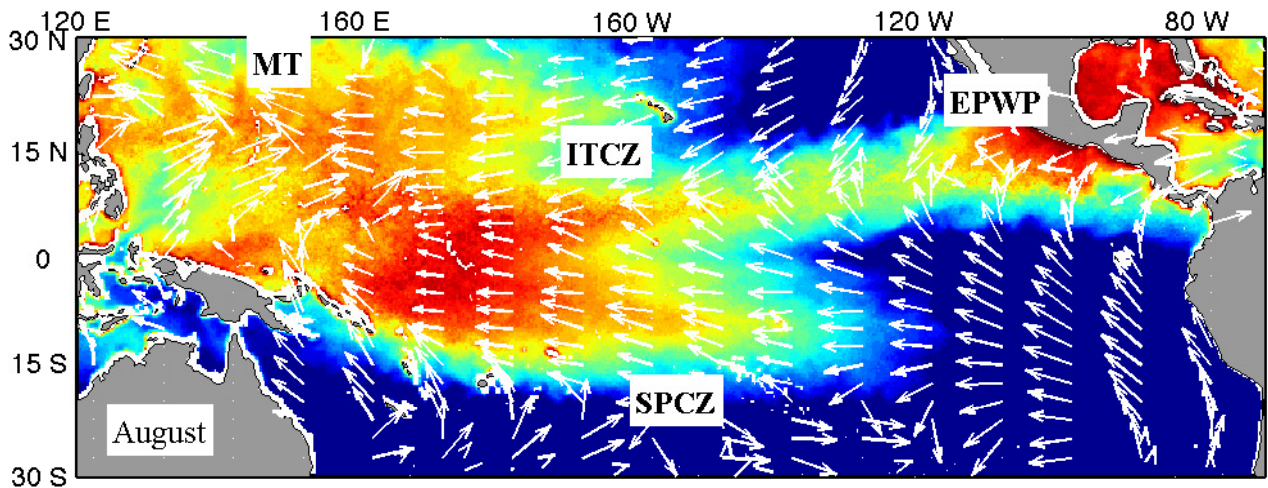


Fig. 1: SST field and superimposed ocean wind vectors for a typical January in the Tropical Pacific. Labels identify the Inter-Tropical and South Pacific Convergence Zones (ITCZ and SPCZ).

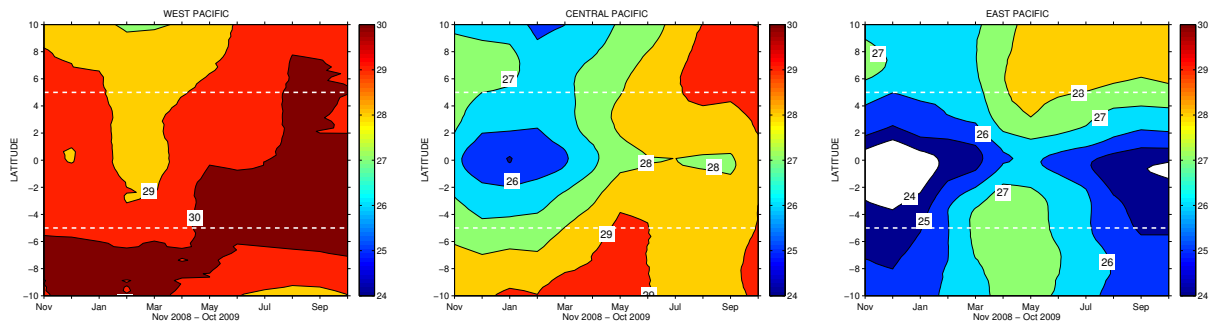


Fig. 2: Latitude-time plots of monthly and zonally averaged SST measured by the TRMM Microwave Imager (TMI) during the study period.

considerable variability in position, shape, and orientation throughout the monsoon season (June–November) ([Lander, 1996](#)). The area near the trough axis is a favorable region for the genesis of tropical cyclones and monsoon depressions.

As boreal summer wanes, the ITCZ migrates southward and across the equator to merge with the SPCZ. As the ITCZ migrates southward, so too does the west Pacific warm pool, defined as the waters enclosed by the 28°C isotherm ([Wyrtki, 1989](#)), an empirical threshold for the onset of deep convection (see Fig. 2). The warm pool spans the western areas of the equatorial Pacific to the eastern Indian Ocean. The high SST in the warm pool creates an environment favorable to the self-organization of individual convection cells into Mesoscale Convective Systems (MCSs) with scales $\sim 300\text{--}400$ km (c.f., [Houze, 2004](#)). These can self-organize into superclusters ($\sim 1000\text{--}3000$ km), which can in turn organize into a large-scale envelope known as the Madden-Julian Oscillation ($\sim 10,000$ km).

The SPCZ is present all year, starting parallel to the equator in the western Pacific before changing direction southeastwards across the Pacific. Convective activity in the SPCZ is greatest during austral summer, so that from November to April frequent and strong convective activity occurs near and just south of the equator. During boreal spring the

area of strongest convergence rapidly moves across the equator and concentrates near the confluence of the ITCZ and MT (10°- 20° N) from May to October (see figure 1 in [Zhu and Wang, 1993](#)).

The southern boundary of the ITCZ in the east Pacific marks the location of a strong SST front that forms the northern boundary of a tongue of cool SST — the east Pacific *cold tongue*. The southern boundary of the cold tongue is formed by another strong SST front. The intensity and spatial extent of the cold tongue varies seasonally ([Mitchell and Wallace, 1992](#)). During the *warm season* (January-June), the ITCZ is nearest the equator and the cold tongue falls to minimum intensity and spatial extent. During the *wet season* (typically March-April) deep convection and rain enter the region. During the *cold season* (July-December), the ITCZ is furthest north and the cold tongue expands, reaching maximum intensity and spatial extent in August-September.

Not shown is another convergence zone that emerges south of the equator in the east Pacific from March to April ([Masunaga and L'Ecuyer, 2010](#), and references therein). This Southern ITCZ is caused by the deceleration of southerly surface winds as they pass over the SST front on the southern boundary of the cold tongue ([Liu and Xie, 2002](#)).

3 Scatterometers and data description

Tab. 1: Orbital parameters. The Equator Crossing Time is the local solar time of the satellite's passage over the equator.

<i>Satellite</i>	<i>QuikSCAT</i>	<i>MetOp-A</i>
Orbital Period	101 min	101 min
Inclination	98.62°	98.59°
Equatorial Crossing Time		
06:30	ascending	–
09:30	–	descending
18:30	descending	–
21:30	–	ascending

The National Aeronautics and Space Administration (NASA) launched the QuikSCAT satellite in June 1999. The mission produced ocean vector winds for more than 10 years, from July 1999 until November 2009. The MetOp-A satellite was launched in October 2006 and is operated by the European Organisation for the Exploitation of Meteorological Satellites (EUMETSAT). Both satellites are in quasi-sun-synchronous orbits. Their local equator crossing times and other orbital parameters are given in Table 1.

The SeaWinds scatterometer is a rotating pencil-beam design with an 1800 km wide swath and transmits at Ku-band (13.4 GHz) ([Tsai et al., 2000](#)). The pencil-beam design has an observation geometry that varies across the swath. This results in a varying performance that is poor in the nadir region and far swath.

The ASCAT scatterometer uses a dual-swath fan-beam configuration with two 550 km wide swaths separated by a nadir gap of about 700 km and transmits at C-band (5.3 GHz) ([Figa-Saldaña et al., 2002](#)). The fan-beam configuration has consistent measurement geometry and instrument performance.

Tab. 2: ASCAT and SeaWinds products.

<i>ASCAT Products</i>	<i>Grid Size (km)</i>	<i>Gridding</i>	<i>Geophysical Model Function</i>	<i>Ambiguity Removal</i>	<i>Constraints</i>
ASCAT-12.5	12.5	centroid binning and Hamming window	CMOD5.n	2DVAR	spatial consistency and meteorological balance
ASCAT-25	25	centroid binning and Hamming window	CMOD5.n	2DVAR	spatial consistency and meteorological balance

<i>Sea Winds Products</i>					
SeaWinds-KNMI	25	centroid binning	NSCAT-2	2DVAR and MSS	spatial consistency and meteorological balance
SeaWinds-NOAA	25	centroid binning	QSCAT-1	MF+DIRTH	wind direction continuity
QSCAT-12.5 (v3)	12.5	Overlap binning	Ku2011	MF+DIRTH	wind direction continuity

3.1 Data

3.1.1 Wind data

The radar backscatter detected by the scatterometers goes through two levels of processing to produce wind speed and wind direction. Level 1 processing involves averaging individual backscatter measurements and produces them on a regularly spaced grid. Level-2 takes the Level-1 data and applies quality control, an inversion step, and an ambiguity removal step. The inversion step applies an empirically derived geophysical model function (GMF) to relate backscatter (as a function of the wind direction) with the equivalent neutral-stability vector wind at a height of 10 meters. Due to the nature of radar backscatter from the ocean surface, this procedure usually provides multiple solutions referred to as ambiguities. An ambiguity removal algorithm is applied to produce the selected winds.

The wind products used in this paper are listed in Table 2. A brief description of the processing used to produce them follows.

ASCAT-12.5 and ASCAT-25 were produced to Level-1 by EUMETSAT. Level-1 cross-section data are calculated by averaging individual backscatter measurements. The weighting function chosen for this averaging is a two-dimensional Hamming window, designed to provide noise reduction and spatial resolution. Level-2 processing is carried out at the Royal Netherlands Meteorological Institute (KNMI) using the ASCAT Wind Data Processor (AWDP). The GMF used in the AWDP is CMOD5.n and ambiguity removal is carried out using a two-dimensional variational method (2DVAR) (*Vogelzang et al., 2009*).

SeaWinds-NOAA is a near-real-time product that was issued by the National Oceanic and Atmospheric Administration (NOAA) and is described in detail by *Hoffman and Leidner (2005)*. Level-1B processing uses a centroid binning method that assigns a backscatter slice to only one WVC. The GMF is QSCAT-1 and ambiguity removal is carried out using a median filter (MF) followed by a sophisticated algorithm called Direction Interval Retrieval with Thresholded Nudging (DIRTH) (*Stiles et al., 2002*) — collectively referred to as MF+DIRTH.

SeaWinds-KNMI is a reprocessing of SeaWinds-NOAA by KNMI using improved (rain) quality control (*Portabella and Stoffelen, 2002*). The GMF is NSCAT-2, and ambiguity removal is carried out using 2DVAR and additional noise reduction by the Multiple Solution Scheme (MSS) (*Vogelzang et al., 2009*).

QSCAT-12.5 (version 3) is the recently released science data product produced by the NASA Jet Propulsion Laboratory (JPL). It is the result of a reprocessing of the entire SeaWinds on QuikSCAT mission with many algorithm improvements (*Fore et al., 2012*). Level-1B processing uses an overlap binning method that increases the number of backscatter slices being assigned to the same WVC. The GMF is Ku2011 and ambiguity removal is carried out using MF+DIRTH.

3.1.2 NWP data

Collocated NWP forecasts are packaged with each product. The SeaWinds-NOAA and QSCAT products are collocated with NWP forecasts from the National Center for Environmental Prediction (NCEP) model. The ASCAT and SeaWinds-KNMI products are collocated with NWP forecasts from the European Centre for Medium range Weather Forecasting (ECMWF) model.

3.1.3 Rain data

Rain affects the radar backscatter measured by scatterometers: the higher the radar frequency, the larger the impact of rain attenuation and scattering. As a result, rain is a larger source of error for winds derived from Ku-band instruments (SeaWinds) than from C-band instruments (ASCAT). For example, as many as 16% of wind retrievals from SeaWinds measurements over the west Pacific warm pool are flagged as rain-contaminated. In contrast, the lower ASCAT radar frequency results in winds that are much less affected by rain, although they are sensitive to secondary effects, such as the splashing of rain drops on the surface and local wind variability when rain is heavy. These secondary effects of rain are a source of ‘geophysical noise’, which at present are not flagged by quality control (*Portabella et al., 2012*).

Rain-rates were obtained from the Tropical Rainfall Measuring Mission’s (TRMM) Microwave Imager (TMI) on board the TRMM satellite. The TMI data were obtained from the Remote Sensing Systems Web site (<http://www.ssmi.com>). We also use SeaWinds Radiometer (SRad) rain-rates. These are derived from SeaWinds measurements of the ocean radiometric brightness temperature (*Laupattarakasem et al., 2005*) and are included with the QuikSCAT 25 km L2B science data product (available from the Physical Oceanography Distributed Data Archive (PO.DAAC)).

3.1.4 Ambiguity removal and noise

MF+DIRTH and 2DVAR approach ambiguity removal differently (*Portabella and Stofjelen, 2004*). The wind retrieval procedure provides local wind ambiguities at varying probability. MF+DIRTH only takes up to four ambiguity direction windows into account with an accumulated probability of 80%, which may lead to some truncation noise (*Stiles et al., 2002*). 2DVAR, on the other hand, considers all wind directions, but with varying probability. That is, 2DVAR takes the full local wind vector probability density function into account at each WVC. MF+DIRTH uses wind direction continuity to constrain the wind retrieval, while the variational approach in 2DVAR ensures spatial consistency and meteorological balance of the retrieved winds.

The main source of noise in wind vector retrieval is caused by rain. The noise is random in the sense that the strength of the effect depends on rain-rate (which is spatially rather variable); moreover, it tends to dominate in the transverse (across-track) wind component. Another noise source is MF+DIRTH, which tends to produce across-track wind vectors in rainy conditions. That is, MF+DIRTH essentially propagates wind direction continuity.

Because ASCAT operates at C-band, it is less sensitive to rain than QuikSCAT. Moreover, ASCAT has a simpler observation geometry, and as a consequence the wind retrieval procedure typically yields two well-defined minima separated by about 180 degrees. This results in a lower noise level for ASCAT compared to QuikSCAT.

3.2 Study areas

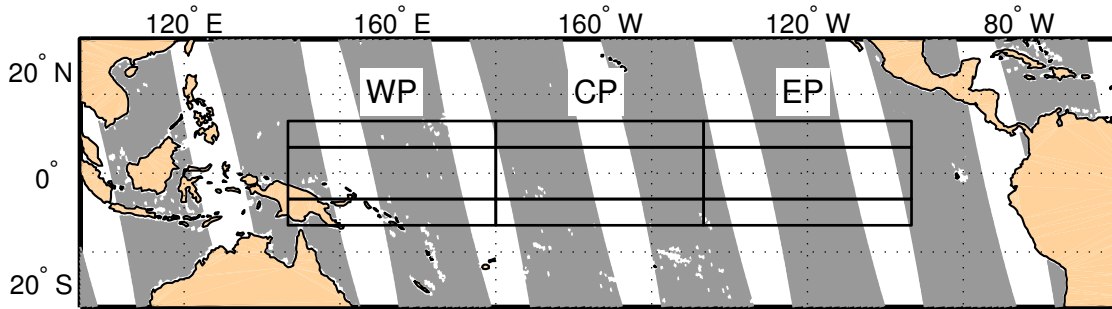


Fig. 3: The boundaries of the nine geographical regions used in the present study. Nomenclature of the regions and their geographical limits are given in Table 3.

Tab. 3: Geographical limits and nomenclature for the regions shown in Fig. 3.

	<i>West Pacific</i> 140° – 180°E	<i>Central Pacific</i> 180° – 220°E	<i>East Pacific</i> 220° – 260°E
<i>North</i> 5° – 10°N	WPN (Rainy)	CPN (Rainy)	EPN (Rainy)
<i>Equator</i> 5°S – 5°N	WPE (Rainy)	CPE (Dry)	EPE (Dry)
<i>South</i> 10° – 5°S	WPS (Rainy)	CPS (Dry)	EPS (Dry)

Figure 3 shows the tropical Pacific subdivided into nine regions; some SeaWinds ascending swaths are shown shaded in grey. The latitude and longitude limits of the regions and their nomenclature are given in Table 3. The lat-lon limits were chosen to facilitate a comparison of structure functions in rainy and dry regions. How well this has been achieved can be judged from the latitude-time plots of TMI rain-rates for the west, central and east Pacific zones (WP, CP and EP) during the study period (Figure 4). Furthermore, because SeaWinds is very sensitive to rain, Figure 4 gives an excellent indication of the expected regional and seasonal variations in the quality of SeaWinds measurements.

The ITCZ can be identified in the figures as a band of heavy rain that persists (or nearly so) throughout the year in CP and EP north of 5°N. In WP there are two rain-rate peaks: one north of the equator (ITCZ peak, centered on 5°N) and one south of the equator (SPCZ peak, between 10°S and 5°S). From May to June the SPCZ peak weakens, while the ITCZ peak strengthens and expands to fill latitudes 5° S to 10°N.

Over a longer period (1999–2010), latitude-time plots of both SST and rain-rate reveal an expansion and contraction of the west Pacific warm pool — the signature of the El

Niño Southern Oscillation (ENSO). During El Niño years (2002–2008 and 2009–2010) the warm pool extends further eastward, causing the SPCZ to have a mainly zonal orientation parallel to the equator. This gives rise to larger rain-rates, particularly in the west Pacific region. During La Niña winters (1999-2000 and 2007-2008) the warm pool contracts and the SPCZ is displaced southwest (*Vincent et al., 2009*). This produces dry conditions and is particularly noticeable in the west Pacific region.

Monthly and regionally averaged SRad rain-rates for morning, evening and combined (ASC+DSC) passes are shown in Figure 5. Comparison with the TMI rain-rates (Fig. 4) show they are in excellent agreement. The SRad rain-rates in the WP (and to a lesser extent in the CP) show an increasing trend. This trend is due to the contraction of the west Pacific warm pool during La Niña in the 2007-2008 winter and its subsequent expansion as El Niño returned in 2009.

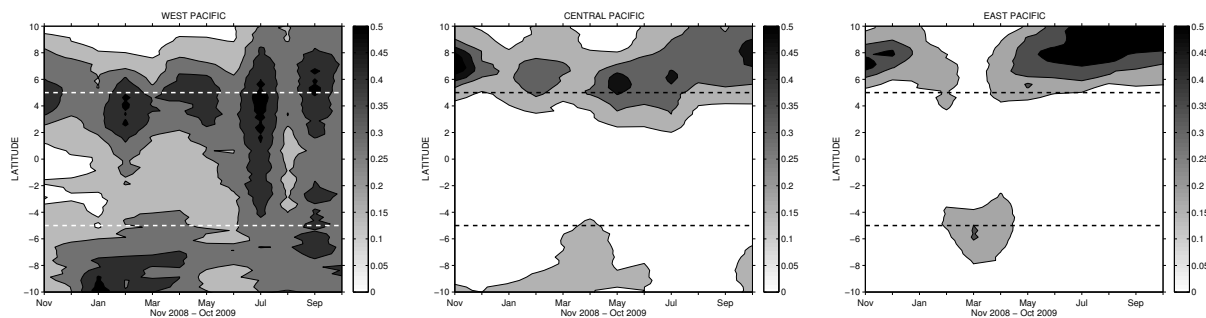


Fig. 4: Latitude-time plots of monthly and zonally averaged rain-rate measured by the TRMM Microwave Imager (TMI) during the study period.

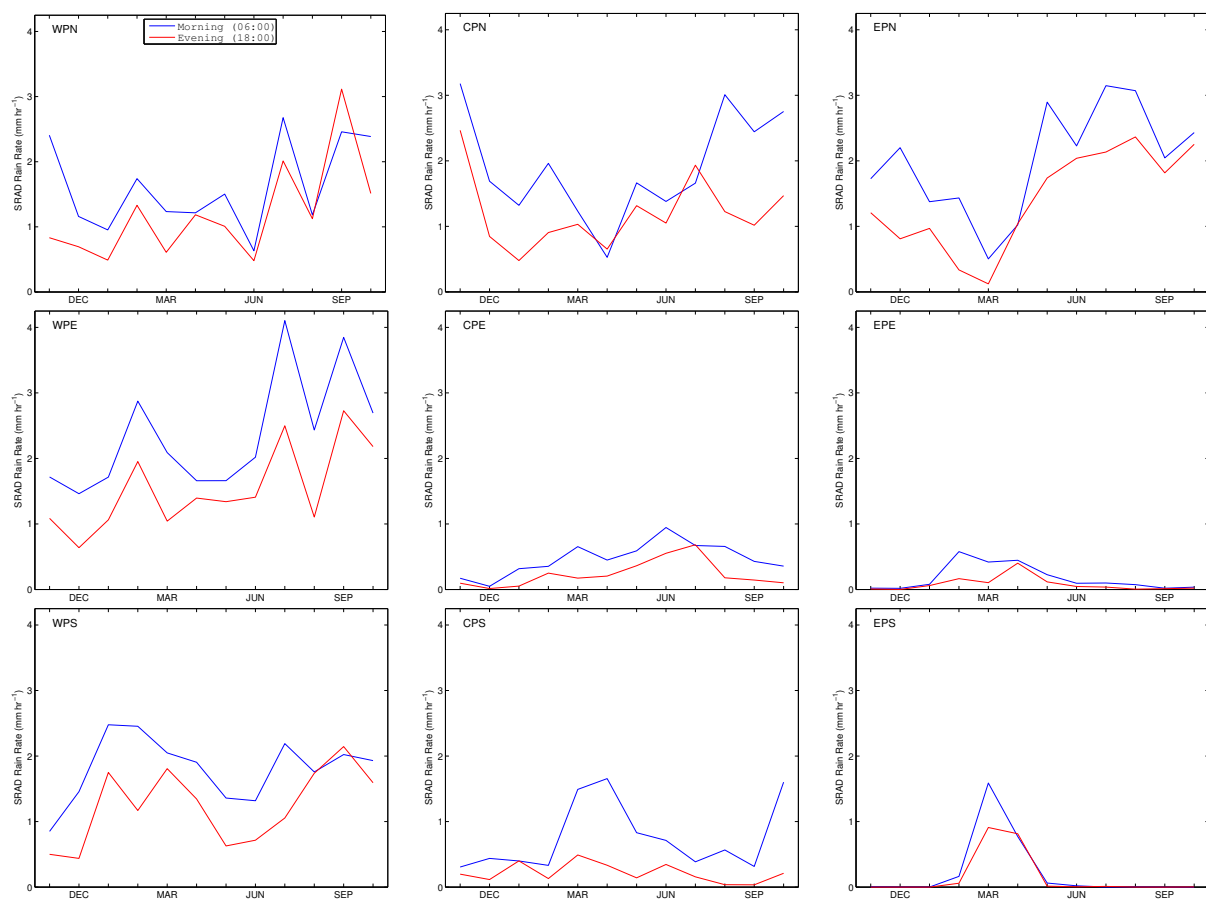


Fig. 5: Box and monthly-averaged SRad rain-rates.

3.3 Samples

Scatterometer wind vectors are organized in a swath grid whose axes are aligned parallel (along-swath) and perpendicular (cross-swath) to the satellite ground track. Each grid point is at the center of a square called a wind vector cell (WVC), and each WVC row corresponds to a single cross-track cut of the measurement swath. The swath is inclined at an angle α relative to the North-South axis that depends on the latitude ϕ and the satellite inclination angle Θ (Table 1) and is given by $\alpha = \pm |\arctan(1/\cos\phi \tan\Theta)|$: positive for the ascending pass (South-to-North), and negative for the descending pass (North-to-South).

Samples were taken along-swath; that is, WVCs in the same sample all have the same cross-swath index. Samples were checked and any wind vectors with coordinates outside the region of interest or that did not pass quality control were flagged as missing. In the case of SeaWinds-NOAA and QSCAT-12.5 wind vectors, wind vectors were flagged missing if the rain flag was set. In the case of ASCAT winds, wind vectors were flagged missing if the KNMI quality control flag or the variational quality control flag was set (see [KNMI, 2011](#), section 6.2). Samples from both the ascending and descending passes of the satellite and from the whole swath (including the outer and nadir parts of the SeaWinds swath) were used.

4 Data Analysis

The most common data analysis tools for studying small-scale turbulence are spatial spectra, correlation functions and structure functions. The assumptions of homogeneity and isotropy enable derivation of certain statistical relationships that can be used to interpret observations and to test turbulence models. Atmospheric motions in the mesoscales (2–2000 km) are constrained by density stratification, rotation and the thinness of the atmosphere. These constraints limit vertical velocities and give rise to stratified turbulence: a form of turbulence that is neither fully three-dimensional nor fully two-dimensional. As a result, the framework of two-dimensional homogeneous isotropic turbulence theory is used to interpret and discuss the results presented here.

4.1 Second-order structure functions

4.1.1 Definitions

The second-order velocity structure function is defined as the covariance of the difference in velocity between two points \mathbf{x} and $\mathbf{x} + \mathbf{r}$. Let $\delta u_i = u_i(\mathbf{x} + \mathbf{r}) - u_i(\mathbf{x})$ denote that difference for velocity component u_i , then

$$D_{ij}(\mathbf{r}) = \langle \delta u_i \delta u_j \rangle, \quad (1)$$

where $\langle \cdot \rangle$ denotes an average over all position vectors \mathbf{x} in the domain. The assumptions of homogeneity and isotropy are used in order to establish some theoretical relationships.

Using those assumptions, space correlations depend only on the distance $r = |\mathbf{r}|$ between the two points and not on their location or the orientation of the line joining them. Then it may be shown that $D_{ij}(\mathbf{r})$ may be expressed in terms of longitudinal (L) and transverse (T) structure functions:

$$D_{ij}(\mathbf{r}) = D_{TT}(r)\delta_{ij} + [D_{LL}(r) - D_{TT}(r)] \frac{r_i r_j}{r^2} \quad (2)$$

where $D_{LL}(r) = \langle \delta u_L \delta u_L \rangle$, $D_{TT}(r) = \langle \delta u_T \delta u_T \rangle$, $D_{LT}(r) = \langle \delta u_L \delta u_T \rangle$, $\delta u_L = \delta \mathbf{u} \cdot \mathbf{e}_L$, $\delta u_T = \delta \mathbf{u} \cdot \mathbf{e}_T$, \mathbf{e}_L and \mathbf{e}_T are unit vectors parallel and orthogonal to \mathbf{r} , and δ_{ij} is the kronecker delta (equal to 1 if $i = j$ and 0 otherwise). The assumption of isotropy means that

$$D_{LT}(r) = 0 \quad (3)$$

4.1.2 Theoretical relationships for 2D turbulence

If the turbulence is isotropic, two-dimensional, and the flow is incompressible flow, then

$$D_{TT}(r) = \frac{d}{dr} [r D_{LL}(r)] \quad (4)$$

In the inertial range, the second-order structure function takes the form ([Lindborg, 1999](#), p. 271)

$$D_{LL}(r) = C |F|^{2/3} r^{2/3} \quad (5)$$

where C is the Kolmogorov constant for 2D turbulence and F is the energy flux. The absolute value of F is taken because energy cascades upscale (i.e. $F < 0$) in two-dimensional turbulence. Substitution of (5) into (4) yields

$$\frac{D_{TT}}{D_{LL}} = \frac{5}{3}. \quad (6)$$

We also mention here that if atmospheric turbulence is due to gravity wave interactions ([Dewan, 1997](#)), the ratio is instead $D_{TT}/D_{LL} = 3/5$ ([Lindborg, 2007](#)).

4.1.3 Relationship with velocity covariance function

The covariance between velocity components at positions \mathbf{x} and $\mathbf{x} + \mathbf{r}$ is defined as

$$R_{ij}(\mathbf{r}) = \langle u'_i(\mathbf{x}) u'_j(\mathbf{x} + \mathbf{r}) \rangle, \quad (7)$$

where $u' = u - \langle u \rangle$. Applying the assumptions of homogeneity and isotropy leads to

$$D_{LL}(r) = 2\sigma_L^2 [1 - \rho_L(r)] \quad (8)$$

$$D_{TT}(r) = 2\sigma_T^2 [1 - \rho_T(r)] \quad (9)$$

where $\sigma_i^2 = R_{ii}(0) = \langle u_i'^2 \rangle$ for $i = L, T$. Note that since $\rho_i = 1$ at $r = 0$ and $\rho_i \rightarrow 0$ as $r \rightarrow \infty$, then

$$D_{ii}(0) = 0, \quad (10)$$

$$D_{ii}(r \rightarrow \infty) \rightarrow 2\sigma_i^2. \quad (11)$$

4.1.4 Relationship with spectra

In homogeneous isotropic turbulence, structure functions and energy spectra are related by ([Babiano et al., 1985](#); [Pope, 2000](#))

$$D_{ij}(r) = 2 \int_0^\infty (1 - \cos kr) E_{ij}(k) dk, \quad (12)$$

where $E(k)$ is the one-dimensional spectral energy density at wavenumber k . Relationship (12) shows that a wave mode which is sharply represented in Fourier space by a single wavenumber is spread over a range of separation distances when represented by the structure function.

4.2 Application to scatterometer winds

Wind vectors are given in terms of horizontal wind speed U and wind direction ϕ_0 measured clockwise from North (oceanographic convention). They are presented in a cross-swath – along-swath coordinate system (x_c, x_a) . Along-swath samples are selected from each orbit. That is, wind vectors in a sample have different x_a but the same x_c . Samples are checked to ensure that only wind vectors with latitude and longitude within the region of interest are used to compute velocity differences. Wind vectors that fail quality control are treated as missing.

After expressing wind direction counter-clockwise from East: $\phi_u = \pi/2 - \phi_o$, longitudinal and transverse wind components are calculated as

$$u_{La} = U \sin(\phi_u - \alpha) \quad (13)$$

$$u_{Ta} = -U \cos(\phi_u - \alpha) \quad (14)$$

where the subscript a is used to indicate that separations are taken along x_a . Then one-dimensional along-swath second-order structure functions are defined by

$$D_{LLa}(r) = \langle \delta u_{La} \delta u_{La} \rangle, \quad D_{TTa}(r) = \langle \delta u_{Ta} \delta u_{Ta} \rangle, \quad D_{LTa}(r) = \langle \delta u_{La} \delta u_{Ta} \rangle \quad (15)$$

where $\delta u_{La} = u_{La}(x_a + r) - u_{La}(x_a)$, and $\delta u_{Ta} = u_{Ta}(x_a + r) - u_{Ta}(x_a)$.

Trend removal Variations in the wind field larger than the region selected for study appear as trends or large-scale inhomogeneities. In a spectral analysis these must be removed using a detrending algorithm; otherwise an erroneous k^{-2} contribution will be added to the spectrum. Because structure functions involve differencing, they are less sensitive to these effects than the spectrum. It is easy to show that the error due to the influence of a linear trend ax is $a^2 r^2$ and hence decreases as $r \rightarrow 0$. Therefore, at small scales the structure function appears to be less vulnerable to trend than the covariance function, and hence spectrum (see [Mahrt and Gamage \(1987\)](#) who discuss this more fully and who found detrending unnecessary for the data they analyzed). In the work reported here, no trend removal is carried out.

5 Structure functions and their characteristics

SeaWinds and ASCAT longitudinal and transverse one-dimensional structure functions for WPE and EPE are shown in Figures 6 (January 2009) and 7 (August 2009). Structure functions for collocated ECMWF-12.5 (dashed black) and NCEP-12.5 (dashed red) winds are included for reference. The figures show that the shapes and amplitudes vary as a function of wind product (indicating differences due to both instrument design and the methods used to retrieve wind speeds and direction), and as a function of region and time of year. In order to compare all 1080 structure functions (five wind products, longitudinal and transverse components, nine regions, and twelve months), it is necessary to devise an efficient strategy.

Turbulence theory leads us to expect that the structure functions for the near-surface wind field should scale like r^β (equivalent to $k^{-(\beta+1)}$ spatial wavenumber spectra). However, Figs. 6 and 7 show that it is not always clear what range of scales to use to estimate the power-law exponent. After inspecting many structure functions, the partitioning indicated by vertical lines was settled on. At the largest scales ($r > 250$ km), the slopes approach those found for NWP models, while at small scales ($\Delta < r \lesssim 50$ km), the effects of spatial filtering and noise can be seen. In the range 50 – 250 km, scatterometers resolve more structure than NWP — the same range of scales occupied by meso-beta weather phenomena, such as squall lines and mesoscale convective systems ([Houze, 2004](#)).

Turbulence theory also identifies the ratio $D_{TT}(r)/D_{LL}(r)$ as an interesting quantity. Assuming isotropic turbulence due to an inertial range energy cascade in 2D, then from Eq. (4) the ratio D_{TT}/D_{LL} would be independent of r and equal to 5/3. Alternatively, if the isotropic turbulence were due to interacting gravity waves, then D_{TT}/D_{LL} would equal 3/5. In either case, the implication is that the longitudinal and transverse structure functions will have identical slopes.

Figure 8 shows D_{TTa}/D_{LLa} as a function of r for the three equatorial regions in January (top) and August (bottom) 2009. In CPE and EPE D_{TTa}/D_{LLa} is approximately independent of r , consistent with theory. However, its value much closer to 3/5, the value expected for a gravity-wave cascade. In WPE, D_{TTa}/D_{LLa} varies strongly with wind product and strongly with r . The reasons for this behavior is related both to the heavy rainfall and deep convection in the west Pacific and to the differences between SeaWinds and ASCAT processing.

Structure functions will be compared below using the following quantities:

Noise Levels – Structure functions for noise-free data are zero at $r = 0$. It will be shown below that in the case of data contaminated by white noise, $D_{iaa}(r = 0)$ is twice the noise variance. Therefore, we define the noise level as one-half the estimated intercept of $D_{iaa}(r)$ with the $r = 0$ axis.

Structure Function Slopes – These are calculated in log-log space over the range $50 < r < 250$ km (the range indicated by the vertical lines in Figs. 6 and 7). We do not make use of the slope behavior at larger scales.

Structure Function Amplitudes – The magnitude of D_{iia} at $r = 300$ km is taken as a proxy for the turbulent kinetic energy contained in scales less than 300 km.

Ratios — Ratios of component noise levels, slopes and amplitudes.

6 Noise Levels

For data contaminated by noise, the second-order structure function is non-zero at $r = 0$ and, in the case of white noise, equal to $2\sigma_n^2$, where σ_n^2 is the variance of the noise (*Curran and Dungan, 1989*). Suppose that measurements m can be written as the sum of ‘truth’ t and noise n :

$$m(x) = t(x) + n(x). \quad (16)$$

Taking differences between measurements at points x and $x + r$, then $\delta m = \delta t + \delta n$. Squaring and ensemble averaging yields the second-order structure function $D_{mm}(r)$:

$$\begin{aligned} D_{mm}(r) &= \langle \delta m \delta m \rangle \\ &= \langle (\delta t + \delta n)^2 \rangle \\ &= \langle \delta t \delta t \rangle + \langle \delta n \delta n \rangle + 2\langle \delta n \delta t \rangle. \end{aligned} \quad (17)$$

$$= D_{tt} + D_{nn} + 2D_{nt}. \quad (18)$$

The noise has the following properties

$$\langle n \rangle = 0 \quad (19)$$

$$\langle n(x+r)n(x) \rangle = \begin{cases} 0 & (r > 0) \\ \sigma_n^2 & (r = 0) \end{cases} \quad (20)$$

$$\langle n(x)t(x) \rangle = 0. \quad (21)$$

Using property (21), we can write

$$D_{mm}(r) = D_{tt}(r) + D_{nn}(r). \quad (22)$$

If both t and n are stationary, they can be written in terms of their variances σ_t^2 , σ_n^2 and autocorrelation functions $\rho_t(r)$, $\rho_n(r)$:

$$D_{tt}(r) = 2\sigma_t^2(1 - \rho_t(r)) \quad (23)$$

$$D_{nn}(r) = 2\sigma_n^2(1 - \rho_n(r)). \quad (24)$$

For uncorrelated noise (20), $\rho_n(0) = 1$, $\rho_n(r > 0) = 0$, and we can write

$$\begin{aligned} D_{nn}(r) &= 2\sigma_n^2 && \text{for } r > 0 \\ &= 0 && \text{for } r = 0 \end{aligned} \quad (25)$$

Near $r = 0$, $\rho_t(r) \approx 1$. Then, using (25), it follows that

$$\lim_{r \rightarrow 0} D_{mm}(r) = 2\sigma_n^2. \quad (26)$$

In words, there is a peak at $r = 0$ equal to twice the height of the noise variance. In the geostatistics literature (where the second-order structure function is known as the variogram), this limiting value of D_{mm} is called the *nugget*.

Estimating the noise level Noise levels can be quantified by estimating the intercept of $D_{iia}(r)$ with the $r = 0$ axis. This is equivalent to the estimation of the height of the discontinuity (noise peak) in the autocorrelation function at the origin, as reported in [Vogelzang et al. \(2009\)](#). To maintain consistency with that work, we define the noise level as

$$\text{noise level} = \frac{1}{2}D_{iia}(0). \quad (27)$$

Following the experience in [Vogelzang et al. \(2009\)](#), two methods will be used to estimate the noise level. The behavior of the structure function in the dissipation range of turbulence argues for a fit to D_{iia} at small r using a symmetric function (i.e., a function that forces zero derivative at $r = 0$). The simplest choice is a symmetric quadratic (SQ), $f_{SQ} = a + cr^2$, which uses the first two values of the structure function: $D_{iia}(\Delta)$ and $D_{iia}(2\Delta)$. However, because separations of 12.5 km are far from the dissipation scales, a better choice might be an asymmetric function (i.e., one that intersects the $r = 0$ axis at an angle). The simplest choice is the asymmetric quadratic (ASQ), $f_{ASQ}(r) = a + br + cr^2$, which uses the first three values of the structure function: $D_{iia}(\Delta)$, $D_{iia}(2\Delta)$ and $D_{iia}(3\Delta)$.

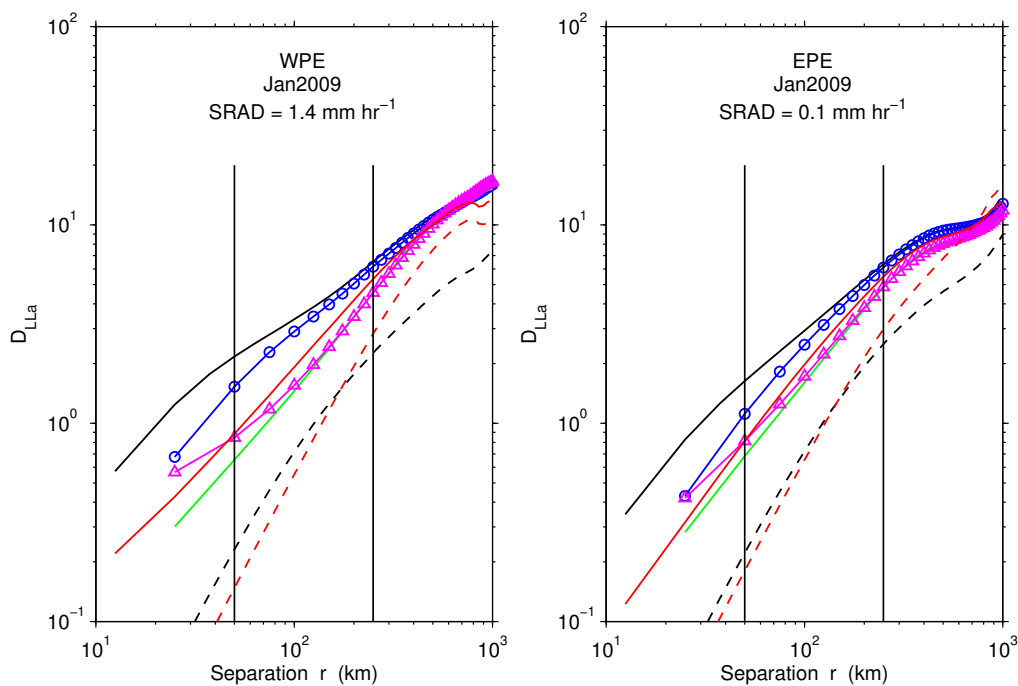
SQ levels Noise levels obtained from the SQ method are shown in Figures 9 (SQ-L) and 10 (SQ-T). The largest SQ-L levels are for SeaWinds-NOAA, consistent with that product having the most rain-related noise ([Vogelzang et al., 2011](#)). Next are ASCAT-25, ASCAT-12.5, SeaWinds-KNMI and then QSCAT-12.5 (4). SQ-L noise levels correlate well with the SRad rain-rates (bar graph) — largest in rainy regions and smallest in dry regions. The SQ-T noise levels vary similarly, with the main difference being that QSCAT-12.5 has a higher noise level than ASCAT and SeaWinds-KNMI.

	<i>SQ noise levels</i>		<i>ASQ noise levels</i>	
	<i>L</i>	<i>T</i>	<i>L</i>	<i>T</i>
ASCAT-25	2	3	5 (-)	4 (-)
ASCAT-12.5	3	4	4 (-)	4 (-)
SeaWinds-KNMI	4	3, 4	3 (+/-)	3 (+/-)
SeaWinds-NOAA	1	1	1	1
QSCAT-12.5	5	2	2 (+/-)	2 (+/-)

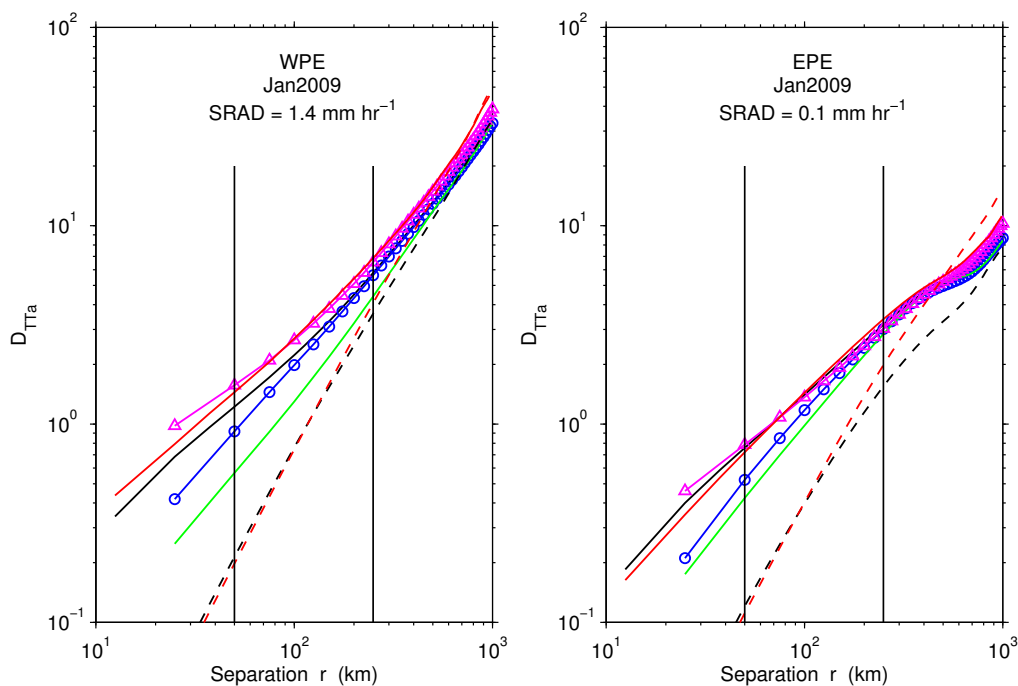
Tab. 4: Ranking of noise levels from largest (1) to smallest (5). The ranking of the SeaWinds-KNMI SQ-T noise level is sometimes larger and sometimes smaller than ASCAT noise levels. SQ levels were always greater than zero, while ASQ levels were either positive or negative (as indicated in parentheses).

Figure 11 compares the SQ noise levels. The T/L ratio (SQ-T/SQ-L) for SeaWinds-NOAA and QSCAT-12.5 is greater than one: the noise in the transverse direction (zonal) component is larger than the longitudinal (meridional) component. On the other hand, both ASCAT products have a T/L ratio less than one, indicating larger noise in the longitudinal direction. SeaWinds-KNMI varies about one, sometimes more like SeaWinds-NOAA and sometimes more like ASCAT. These results are consistent with the triple collocation analysis by [Vogelzang et al. \(2011\)](#), which used buoys that were mostly around the equator and in our study area.

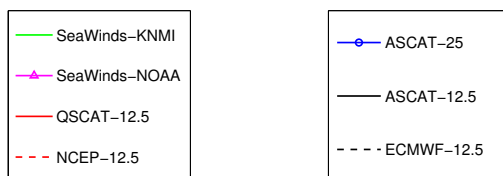
Although there is a clear correlation of noise level with rain-rate for each horizontal component, there is no consistent correlation with the T/L ratio. For example, in EP-North T/L ratios are larger when rain-rate is low, while in EPE ratios are larger when rain-rate is large. In other regions there is no correlation between T/L ratios and rain-rate (e.g., WP).



(a) Longitudinal structure functions.

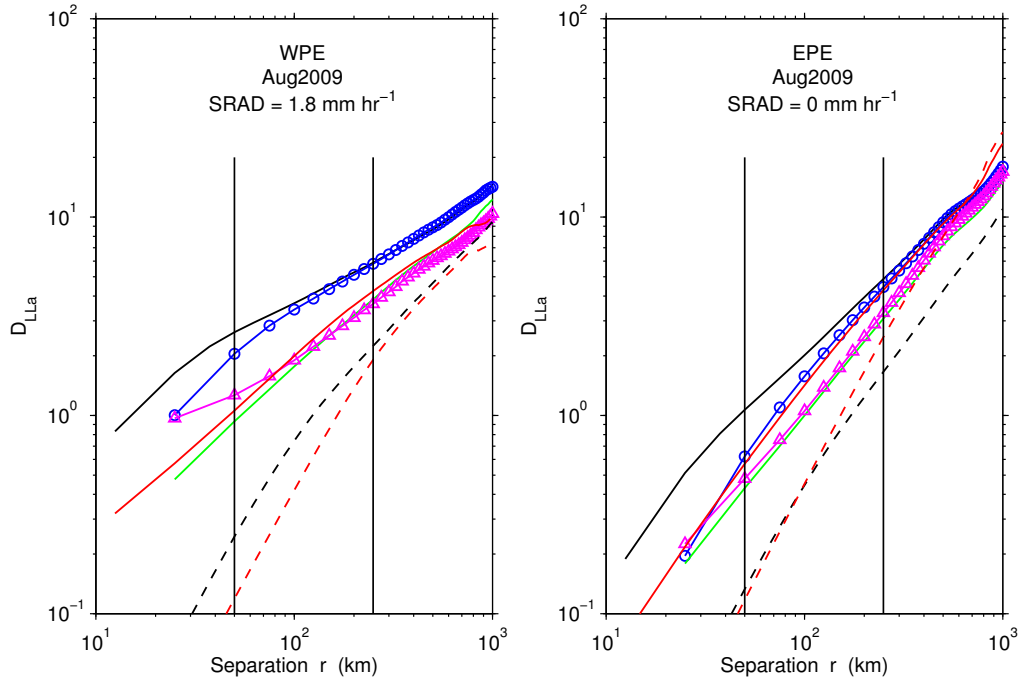


(b) Transverse structure functions.

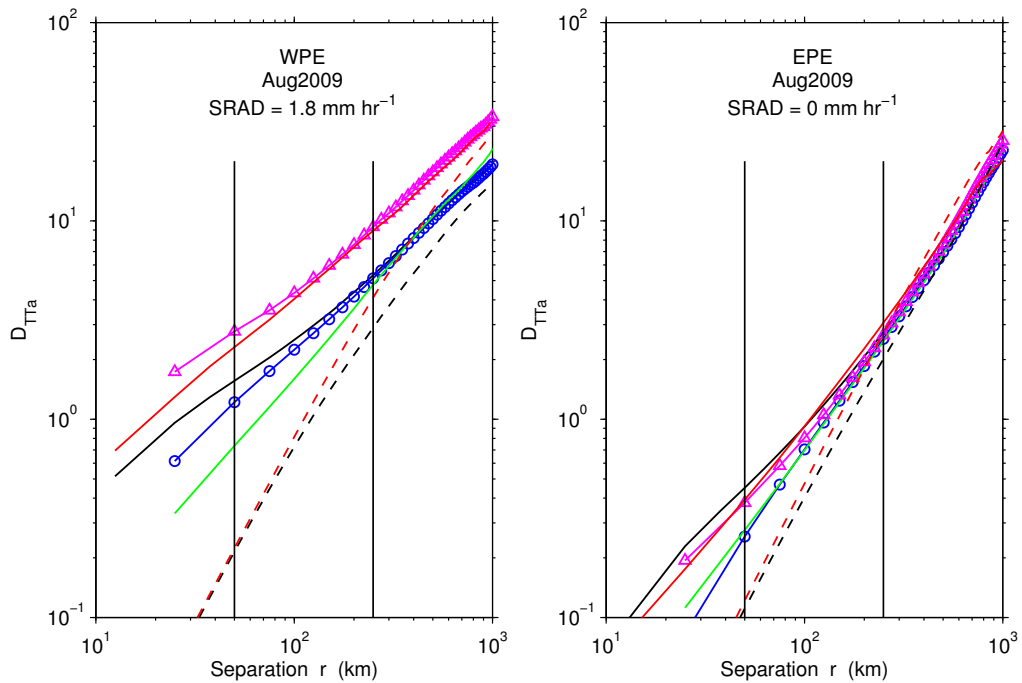


(c) Figure legend.

Fig. 6: Structure functions for the equatorial regions (a) Longitudinal and (b) Transverse; West Pacific (left) and East Pacific (right). The vertical lines are drawn at 50 and 250 km.



(a) Longitudinal structure functions.



(b) Transverse structure functions.

Fig. 7: Same as Fig. 6, but for August 2009.

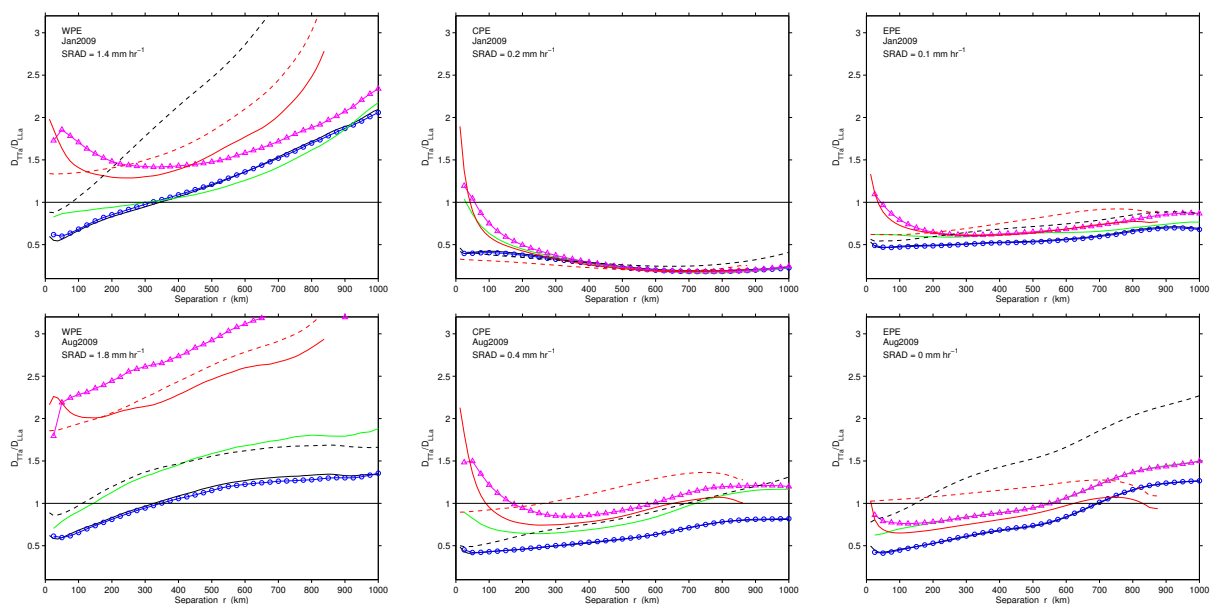


Fig. 8: $D_{TTa}/D_{LL\alpha}$ vs. separation r in the Equatorial regions. Top: January 2009; Bottom: August 2009.

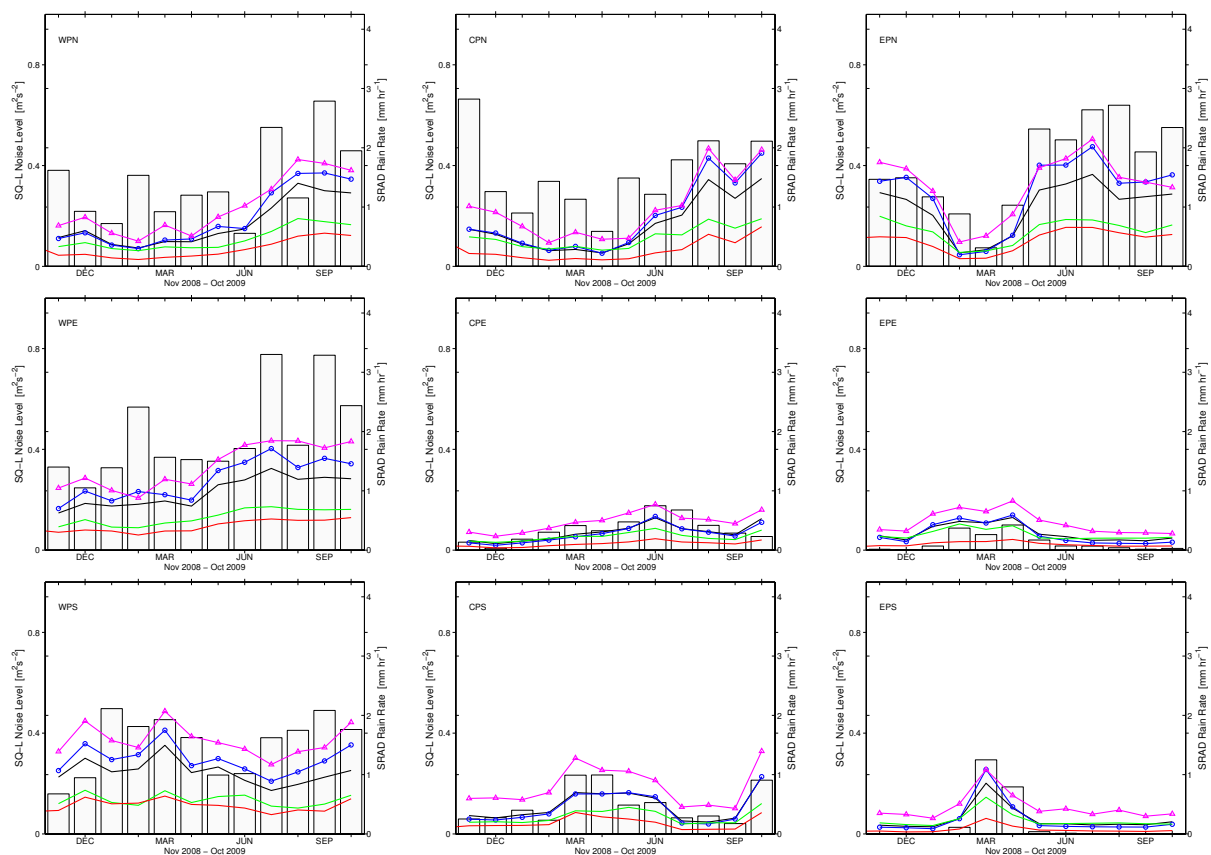


Fig. 9: SQ-L noise levels (from fits to a symmetric quadratic fit) and SRad rain-rates (bars) .

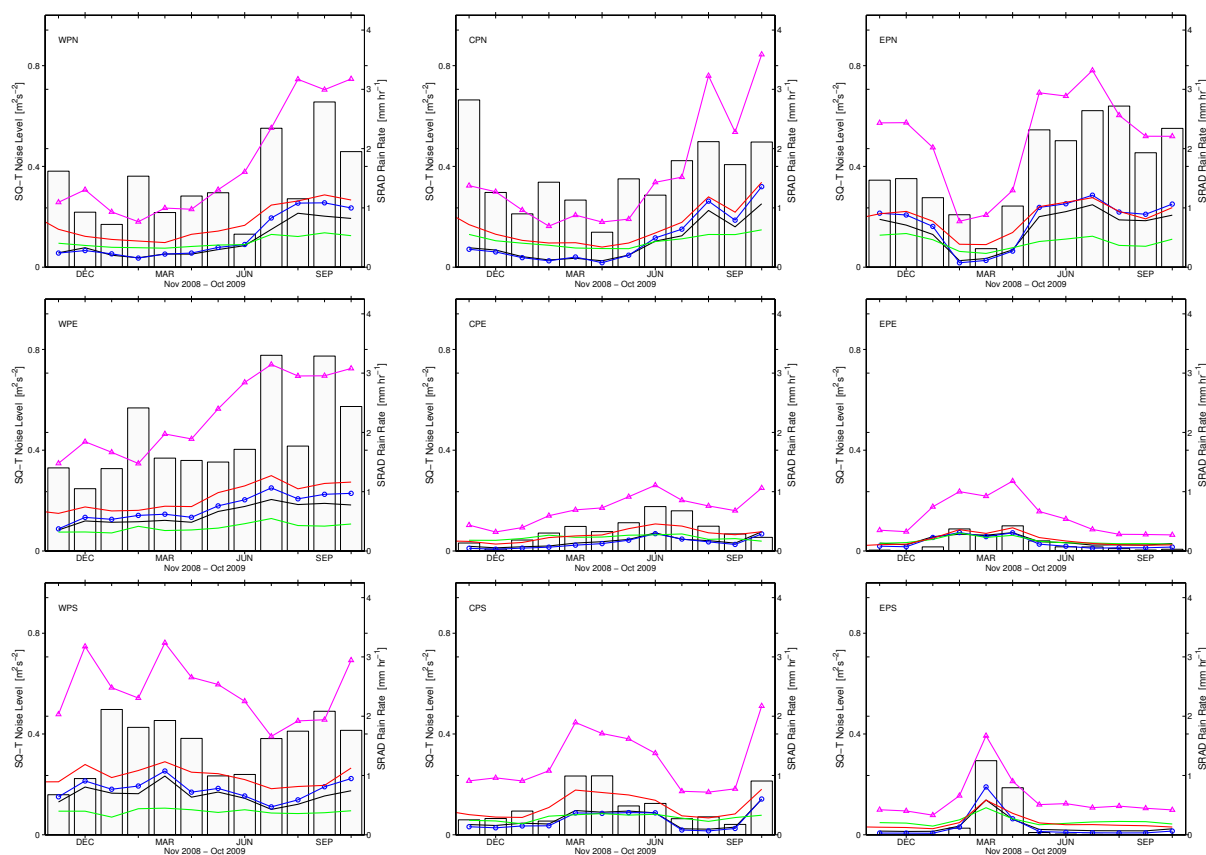


Fig. 10: SQ-T noise levels and SRad rain-rates (bars).

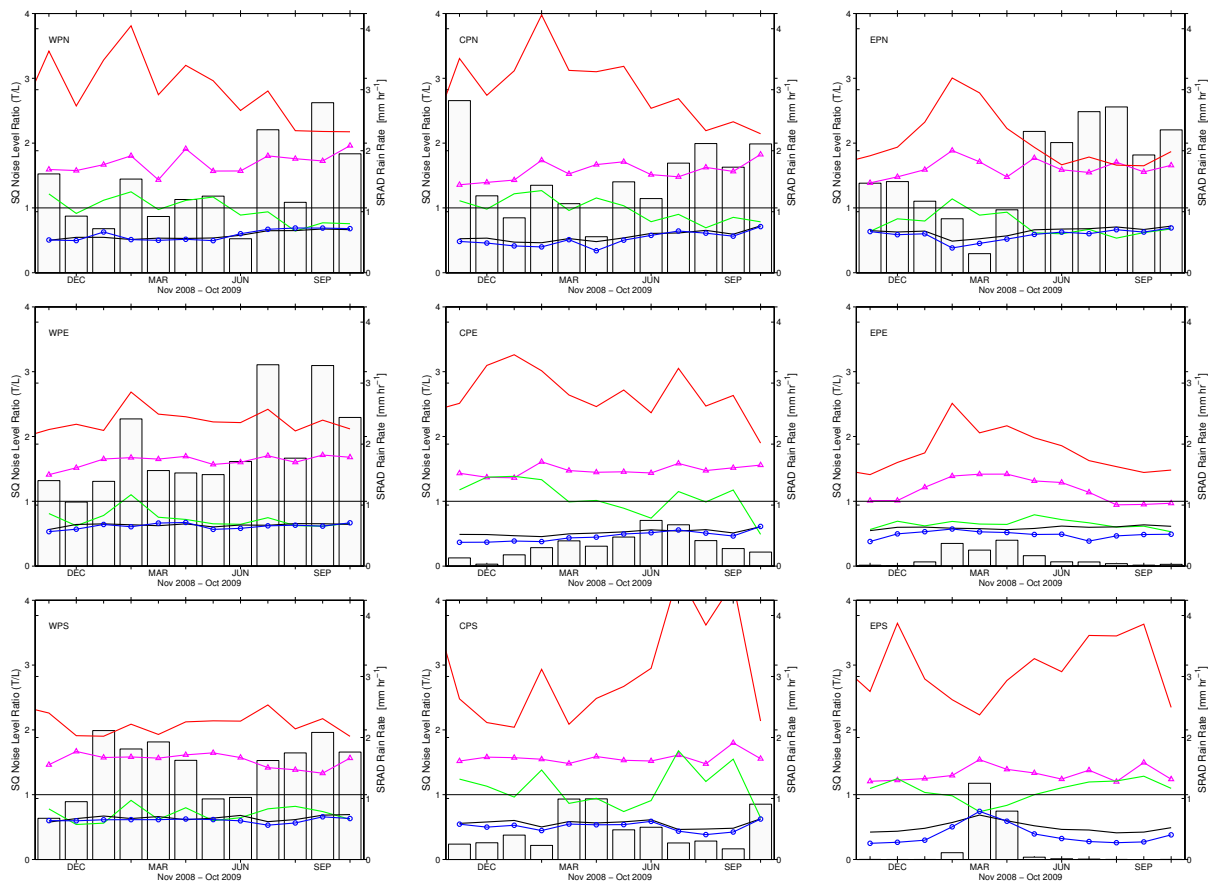


Fig. 11: SQ noise level ratios (T/L).

ASQ levels Noise levels obtained from the ASQ method are shown in Figures 12 (ASQ-L) and 13 (ASQ-T). Like the SQ levels, the SeaWinds-NOAA ASQ levels are large and well-correlated with the rain-rate. However, unlike the SQ levels, the ASQ levels for all other wind products are or are nearly independent of rain-rate. ASQ levels for SeaWinds-KNMI and QSCAT-12.5 are small and oscillate about zero. The ASQ levels for both ASCAT products are negative, with ASQ-L levels (between -0.1 and -0.2) more negative than ASQ-T levels (between 0 and -0.1).

To understand how a noise level be negative, consider the following. When processing the raw radar backscatter, some spatial filtering is applied to reduce noise. A spatial filter of width Δ_f applied to the raw backscatter will attenuate the variance over a distance Δ_f , removing both small-scale signal and small-scale noise. As a result, D_{ia} will be reduced at all distances r and a fit to the structure function near $r = 0$ may result in either positive or negative values for the intercept at $r = 0$. Thus a negative noise level suggests that the filter is too severe, while a positive noise level suggests it is too weak. Based on this, we conclude that the spatial filtering in ASCAT processing is too strong.

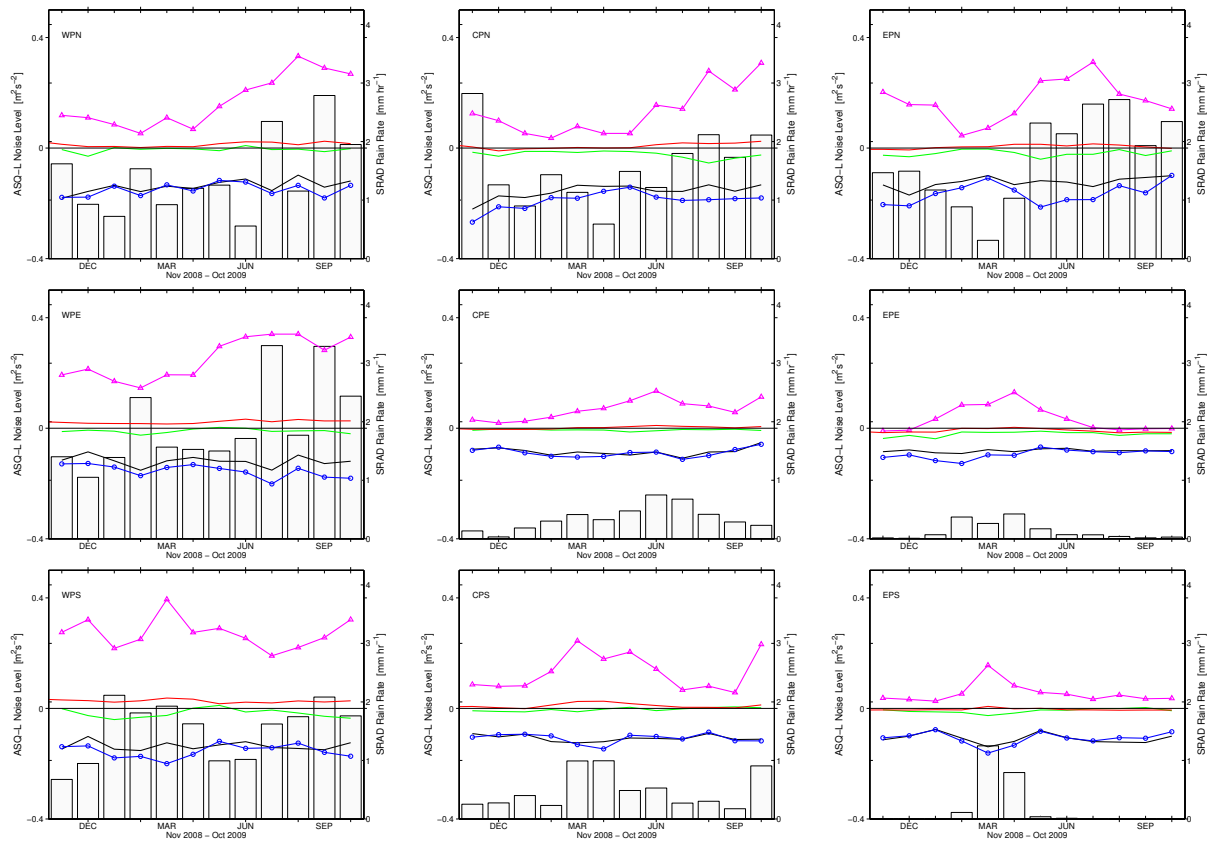


Fig. 12: ASQ-L noise levels (from fits to an asymmetric quadratic) and SRad rain-rates (bars).

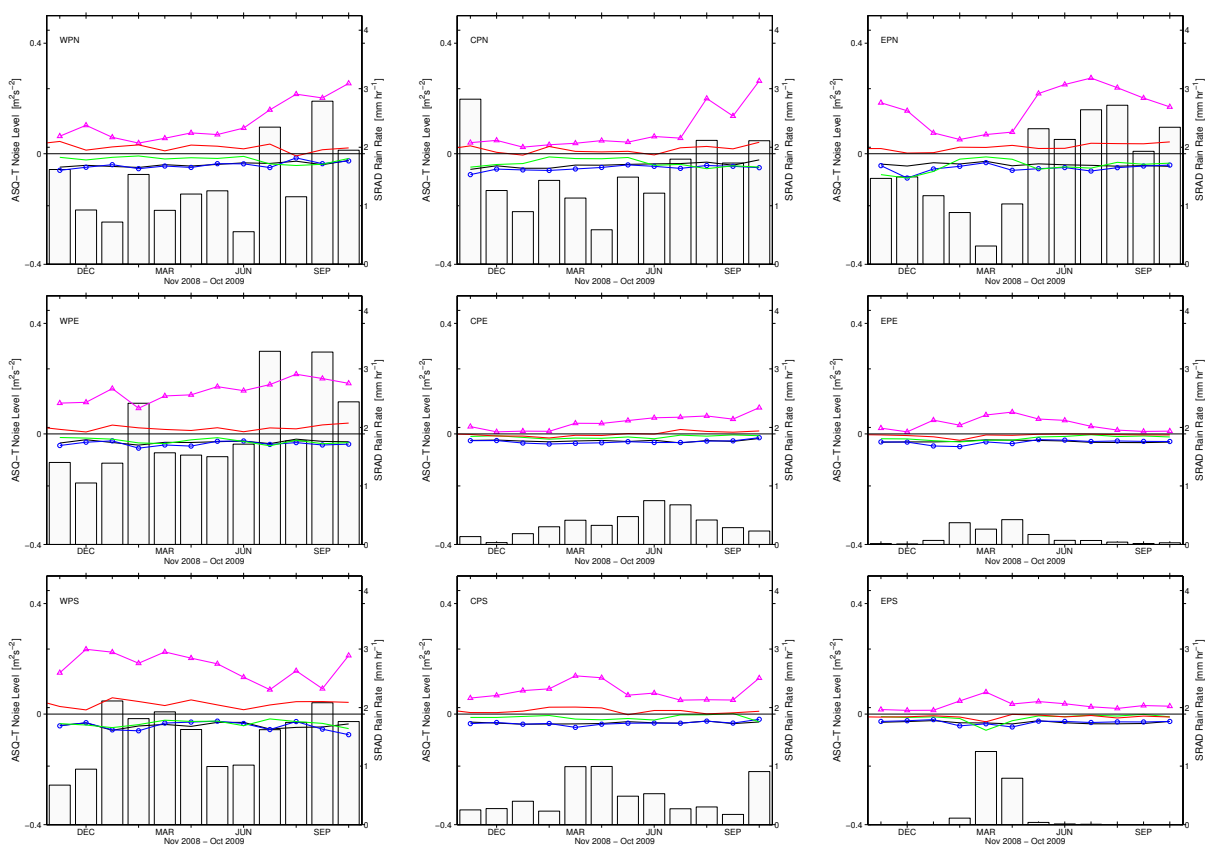


Fig. 13: ASQ-T noise levels and SRad rain-rates (bars).

7 A proxy for the turbulent kinetic energy

Turbulence is comprised of a sea of eddies: compact regions of rotational flow separated from the background by sharp vorticity gradients. Studies of random arrays of model eddies led [Townsend \(1976\)](#) to argue that, to first order, structure functions and energy spectra are related by

$$D_{ii}(r) = \int_{1/r}^{\infty} E_{ii}(k) dk + \dots \quad (28)$$

That is, the turbulent kinetic energy contained in scales less than scale r is approximately equal to $D_{ii}(r)$. However, it is important to remember that (28) is a hypothesis and its accuracy is unknown for isotropic turbulence in general ([Davidson and Pearson, 2005](#)), and for ocean vector winds in particular.

For convenience, let K_{ia} denote $D_{iaa}(300\text{ km})$. Then assuming that (28) is a good approximation, K_{La} and K_{Ta} are proxies for the longitudinal and transverse turbulent kinetic energy contained in the small mesoscales.

Figures 14 and 15 show the dependence of K_{La} and K_{Ta} , respectively, on wind product, region and time of year. Results for different wind products are in excellent qualitative agreement, rising and falling together. The smallest values are in the dry regions and the largest in CP- and EP-North. Differences between ASCAT and SeaWinds products are largest in the rainy regions. The divergent energy K_{La} is larger for ASCAT than SeaWinds throughout the year (and during rainy periods in the dry regions). However, differences in the shear energy K_{Ta} are confined to the tropical cyclone season (June-November in the Northern Hemisphere and December-June in the Southern Hemisphere), when K_{Ta} is much larger for SeaWinds-NOAA and QSCAT-12.5 than ASCAT and SeaWinds-KNMI.

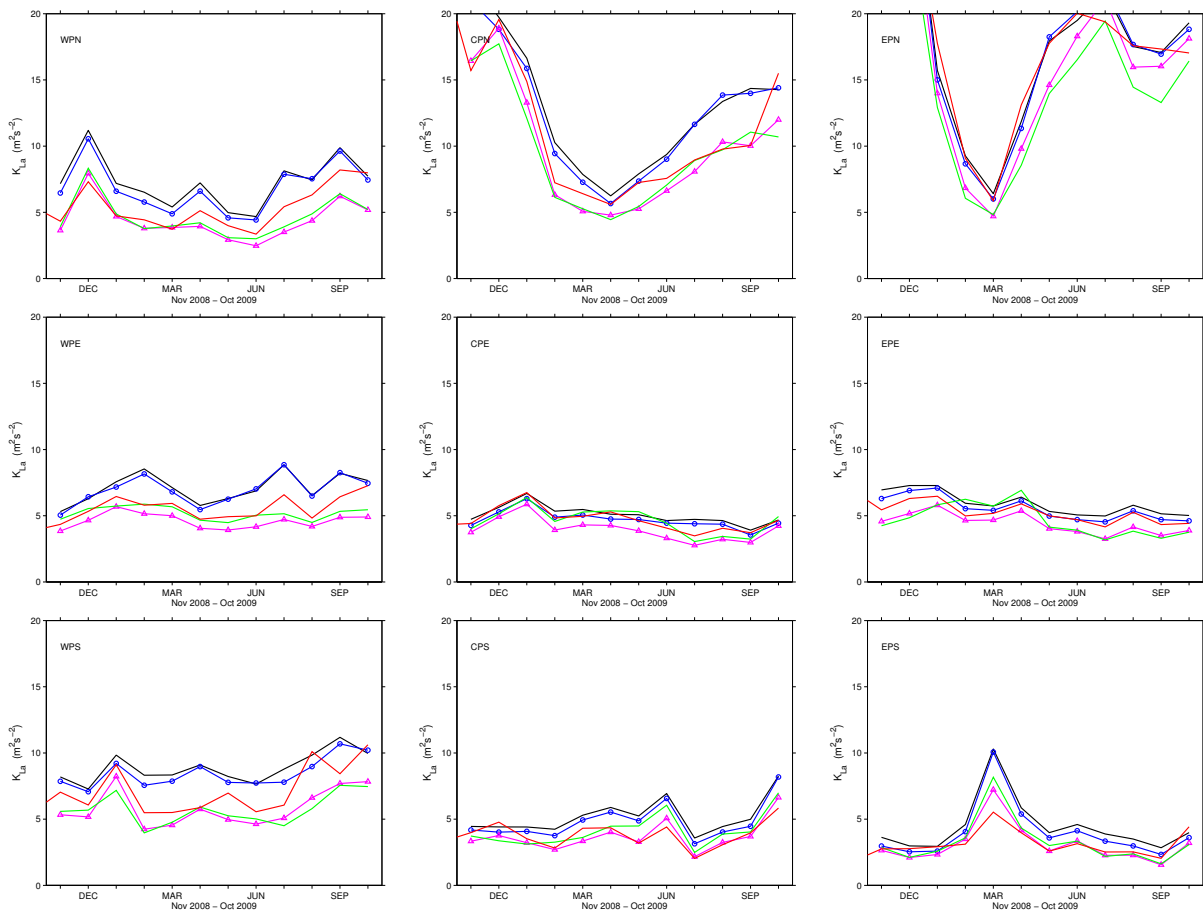


Fig. 14: Mesoscale turbulent kinetic energy K_{La} as a function of month and wind product. The color coding is the same as used in Fig. 6.

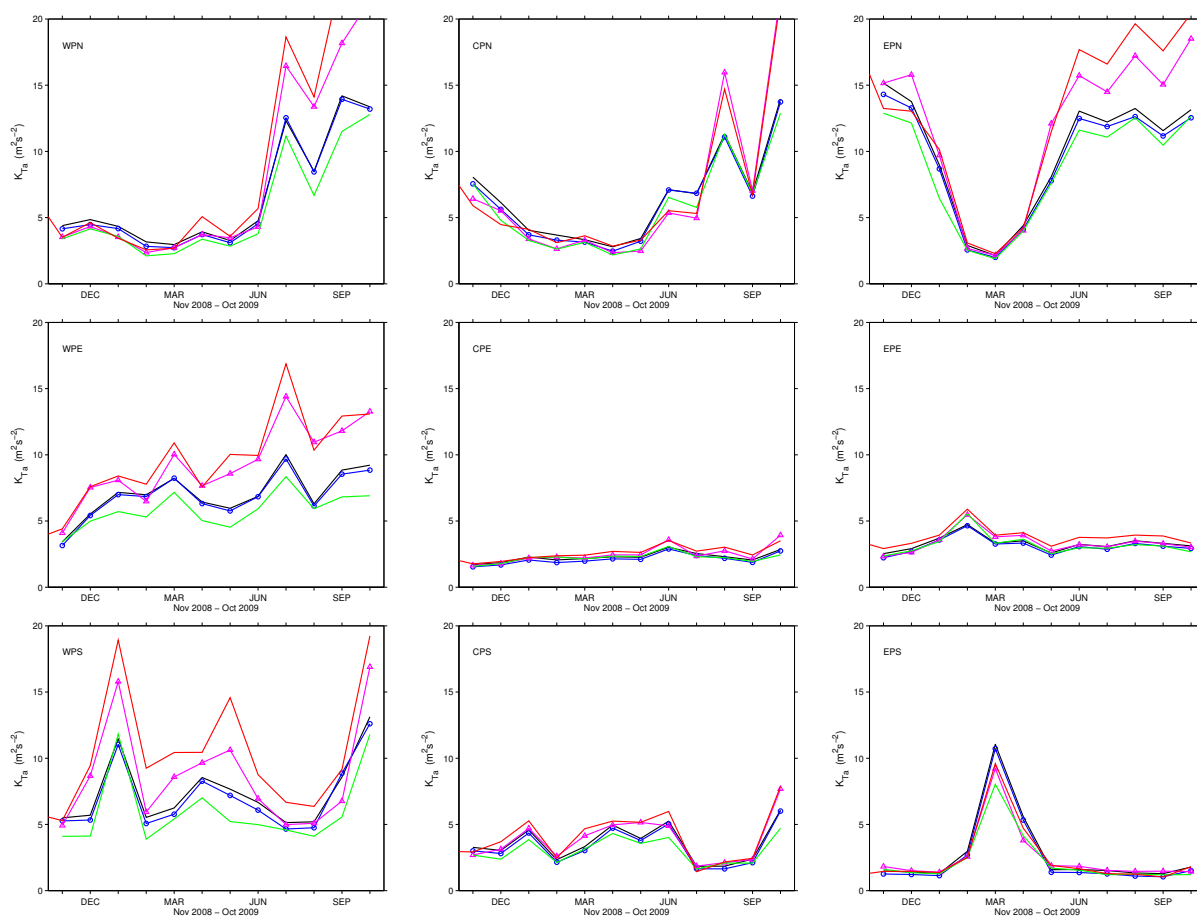


Fig. 15: As in Fig. 14, but for K_{Ta} .

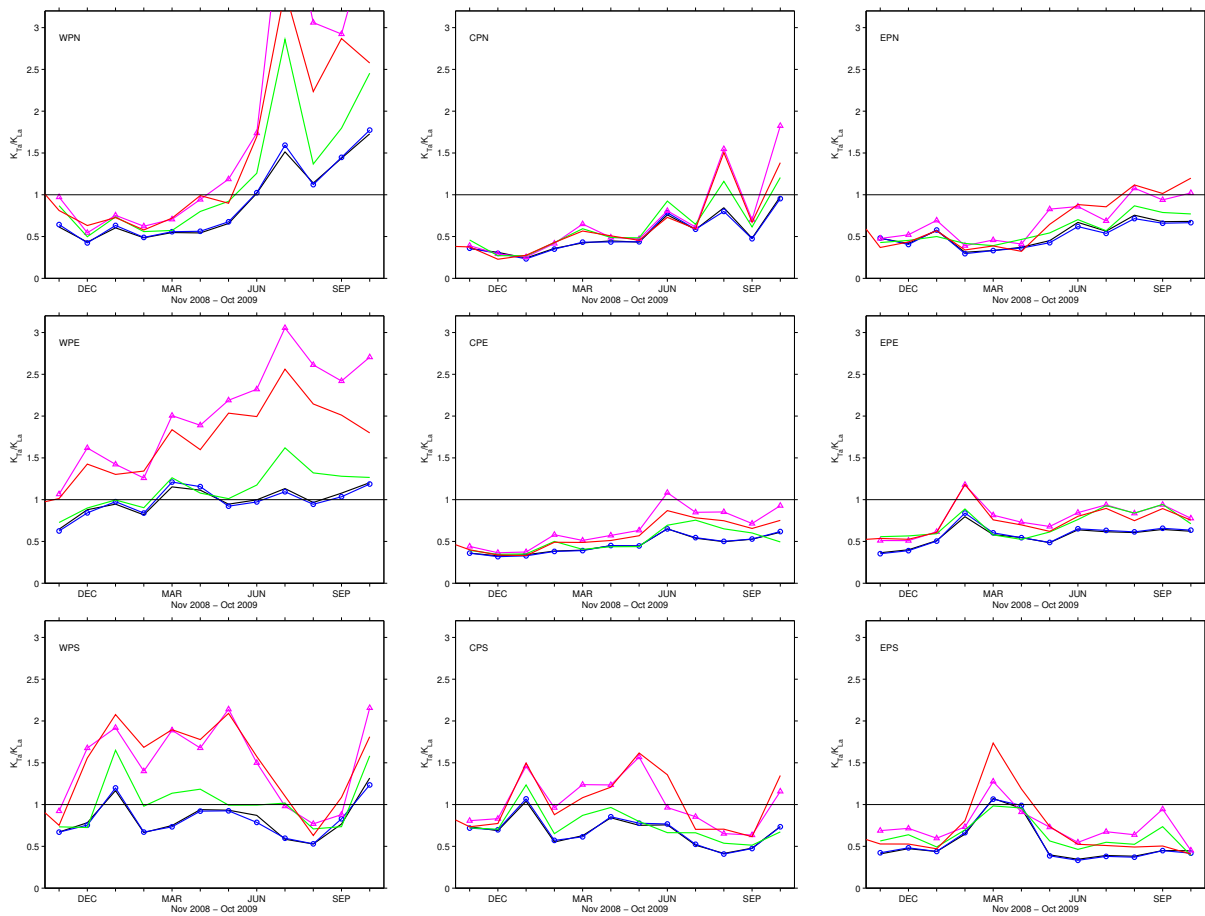


Fig. 16: The monthly variability of vorticity-to-divergence as measured by the ratio K_{Ta}/K_{La} .

A measure of vorticity-to-divergence The ratio of the transverse-to-longitudinal structure function provides a measure of the ratio of vorticity-to-divergence. This can be seen as follows. At small r , $\delta u_L/r \simeq \partial u_L/\partial x_L$ and $\delta u_T/r \simeq \partial u_T/\partial x_L$. This leads us to consider $D_{LLa}(r)$ and $D_{TTa}(r)$, respectively, as indicators of the mean-square meridional divergence and shear at scale r , and hence D_{TTa}/D_{LLa} as a scale-dependent ratio of vorticity-to-divergence. Fig. 8 indicates that the variation of vorticity-to-divergence over time could be monitored at any r greater than about 100 km. Indeed, plots of D_{TTa}/D_{LLa} at $r = 150, 300$ and 600 km all yield similar results. Therefore, we use the ratio at 300 km: K_{Ta}/K_{La} .

Figure 16 shows that for both dry and rainy regions, K_{Ta}/K_{La} is larger for SeaWinds than ASCAT — especially in all WP regions and in CPS. Overall, SeaWinds and ASCAT are in closest agreement when $K_{Ta}/K_{La} < 1$ and in greatest disagreement when $K_{Ta}/K_{La} > 1$. From a dynamical point of view, SeaWinds products indicate more vorticity than ASCAT products — especially in WP.

8 Structure Function Slopes

Structure function slopes are estimated from straight-line fits to $D_{ii}(r)$ in log-log space over the range 50–250 km. Figures 17 and 18 show the longitudinal and transverse slopes, β_L and β_T , respectively. For reference, a horizontal line is drawn at the classical Kolmogorov slope 2/3. Error bars (\pm root-mean-square deviation) for the slopes are also shown.

Curves of β_L and β_T are approximately parallel, indicating good qualitative agreement across wind product. The slopes suggest that β_L has a simpler seasonal variability than β_T . Close inspection of the curves of β_L in Fig. 17 shows that:

1. In general, β_L is smaller in convectively-active months and larger in dry or relatively dry months.
2. ASCAT slopes are flatter than SeaWinds slopes (i.e., $[\beta_L]_{ASCAT} < [\beta_L]_{SeaWinds}$).
3. ASCAT-25 slopes are steeper than for ASCAT-12.5
4. QSCAT-12.5 slopes are usually (but not always) steeper than SeaWinds-NOAA but flatter than SeaWinds-KNMI.

and inspection of the curves of β_T in Fig. 18 shows that:

1. In convectively active months β_T sometimes smaller and sometimes larger. Larger values occur in regions and months with tropical cyclones, and in the EP-Equator due to the development of a planetary wave forced by the meanders of the SST fronts that border the cold tongue (Xie *et al.*, 1998).
2. QSCAT-12.5 slopes are (usually) larger than SeaWinds-NOAA but smaller than SeaWinds-KNMI.
3. ASCAT-12.5 slopes are larger or equal to QSCAT-12.5, except in EP-North during the tropical cyclone season and in EP-Equator during the dry season.

The results of Figs. 17 and 18 are combined in terms of the ratio β_T/β_L in Figure 19. For reference, the ratio for isotropic turbulence (easily derived from relation (4)) is indicated by the horizontal line $\beta_T/\beta_L = 1$. The results separate into three distinct groups: (i) ASCAT-25 and ASCAT-12.5 β_T/β_L near or greater than one, (ii) SeaWinds-NOAA and QSCAT-12.5 β_T/β_L near or less than one, and (iii) SeaWinds-KNMI in a group on its own mid-way between the other two.

The grouping and ratios are consistent with the SQ- T/L ratios shown in Fig. 11. That is, larger noise in the cross-track (zonal) than the along-track (meridional) wind component means that D_{TT} would flatten more than D_{LL} . A slope ratio less than one is consistent with this. QSCAT-12.5 follows SeaWinds-NOAA, an indication that QSCAT-12.5 is also noisy. That is no surprise, as noise is introduced by the ambiguity removal method — although that has been improved for QSCAT-12.5.

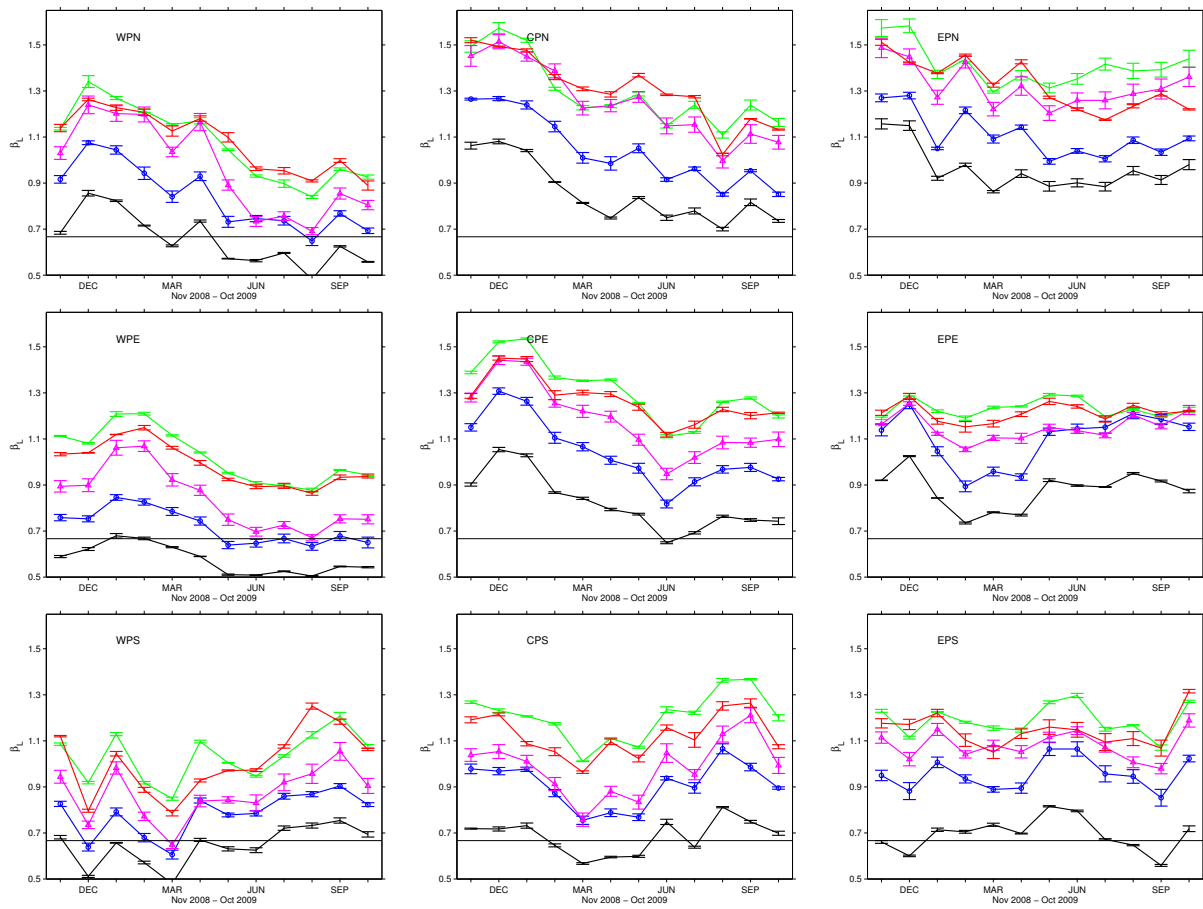


Fig. 17: Monthly variability of β_L and dependence on wind product.

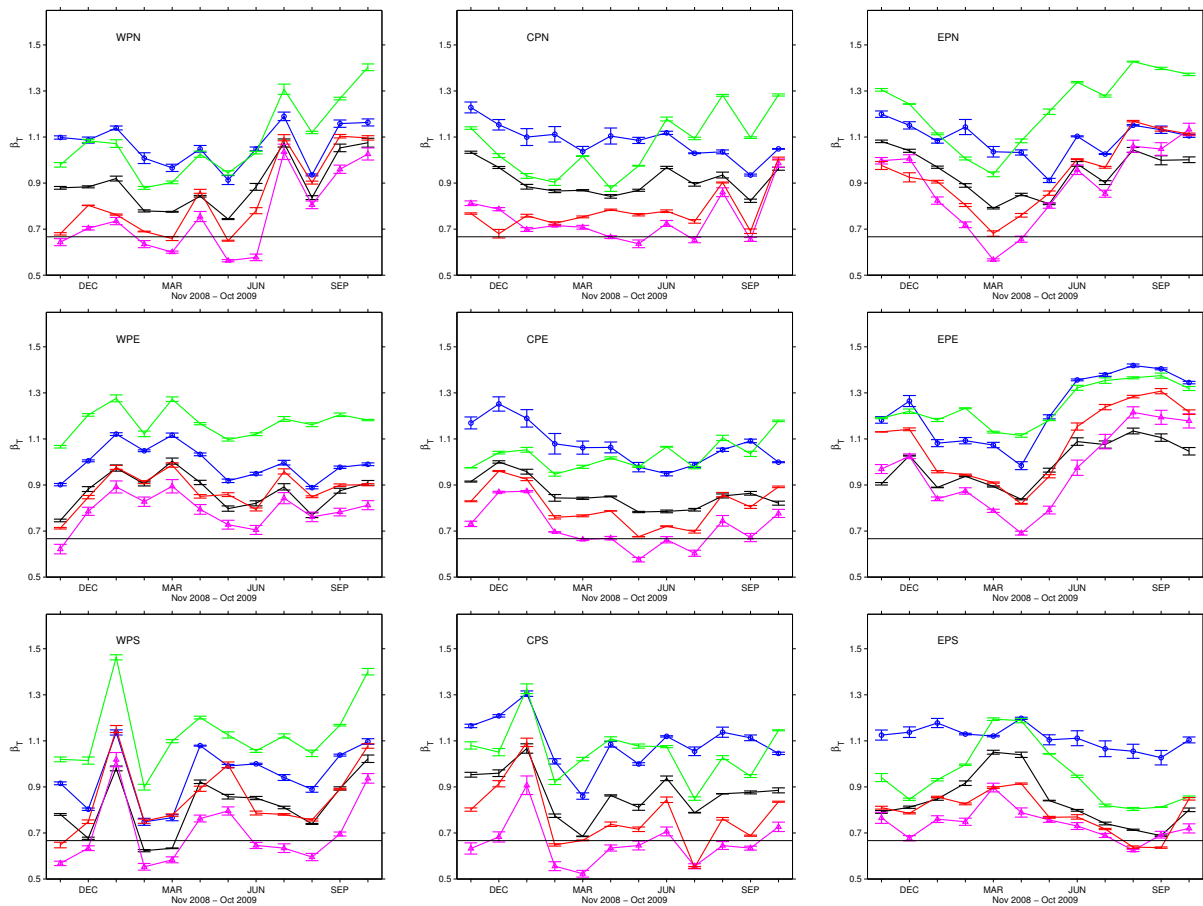


Fig. 18: Monthly variability of β_T and dependence on wind product.

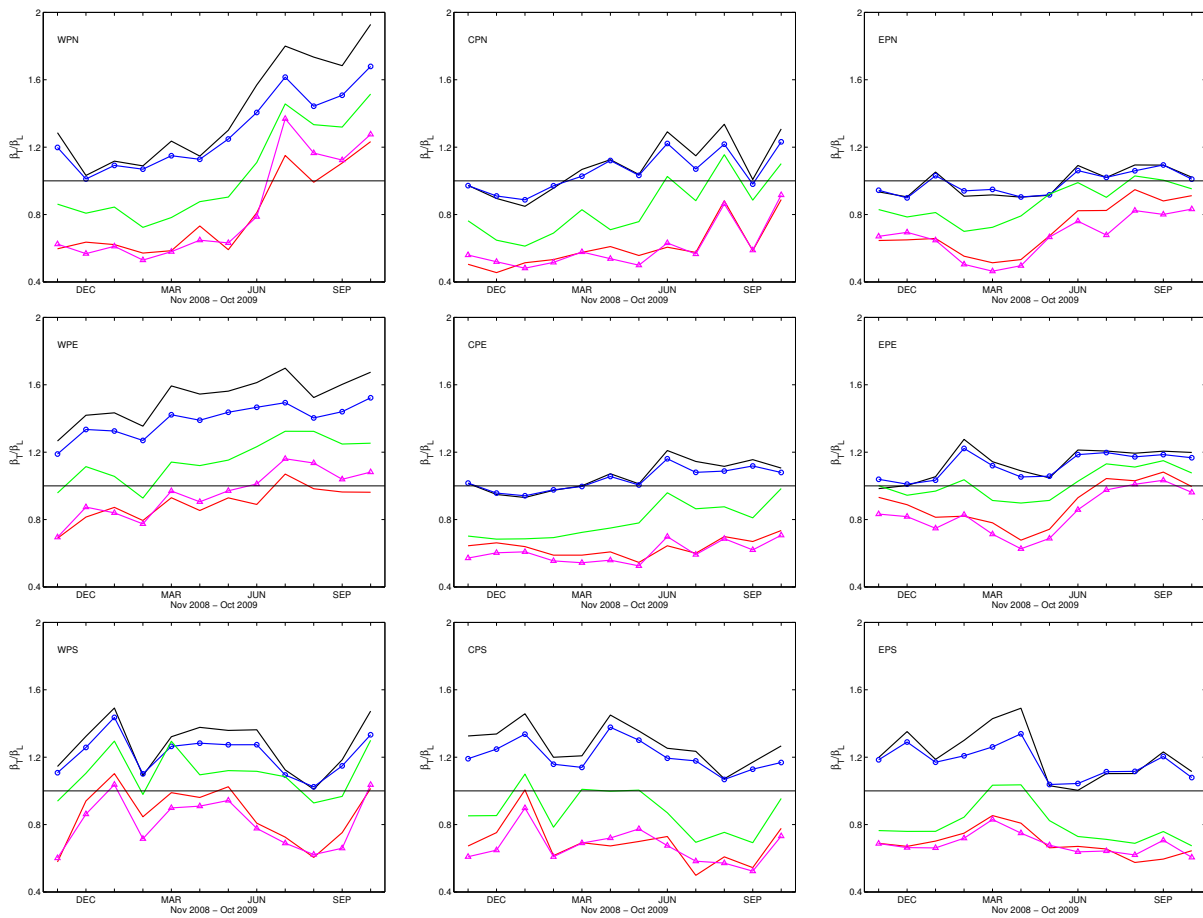


Fig. 19: Slope ratios β_T/β_L .

9 A note on OMB structure functions

Here we present some structure functions for the observations - background (OMB) ocean vector wind field. OMB structure functions should be useful in data assimilation.

Denote the u component of the scatterometer wind at position \mathbf{x} by $u^o(\mathbf{x})$, the NWP wind by $u^b(\mathbf{x})$, and their difference by

$$u^{omb}(\mathbf{x}) = u^o(\mathbf{x}) - u^b(\mathbf{x})$$

The OMB velocity differences are

$$\begin{aligned} \delta u_i^{omb} &= u_i^{omb}(x+r) - u_i^{omb}(x) \\ &= \delta u_i^o - \delta u_i^b \end{aligned}$$

Second-order velocity structure functions for OMB are defined by

$$D_{ij}^{omb}(r) = \langle \delta u_i^{omb} \delta u_j^{omb} \rangle$$

The assumptions of homogeneity and isotropy lead to

$$D_{ii}^{omb}(r) = 2 \left(\sigma_i^{omb} \right)^2 \left(1 - \rho_i^{omb}(r) \right)$$

These relations suggest that if the OMB structure functions approach a constant value at large values of r , then the autocorrelation of OMB goes to zero, which in turn implies that the background error correlation goes to zero. In regions where this happens, background errors affect only a limited area. It is then possible to estimate the background error correlation and use it in 2DVAR following the approach of [Vogelzang and Stoffelen \(2012\)](#). This may open the way to some form of 'dynamic' 2DVAR that adjusts itself to the meteorological conditions. This would be an important result for the NWPSAF.

OMB structure functions for ASCAT-12.5 OMB structure functions are calculated for ASCAT-12.5 using collocated ECMWF first guess fields as background. Results are shown for January 2009 (Figs. 22 and 21) and August 2009 (Figs. 22 and 23).

OMB structure functions for QSCAT-12.5 OMB structure functions are calculated for QSCAT-12.5 using collocated NCEP first guess fields as background. Results are shown for January 2009 (Figs. 26 and 25) and August 2009 (Figs. 26 and 27).

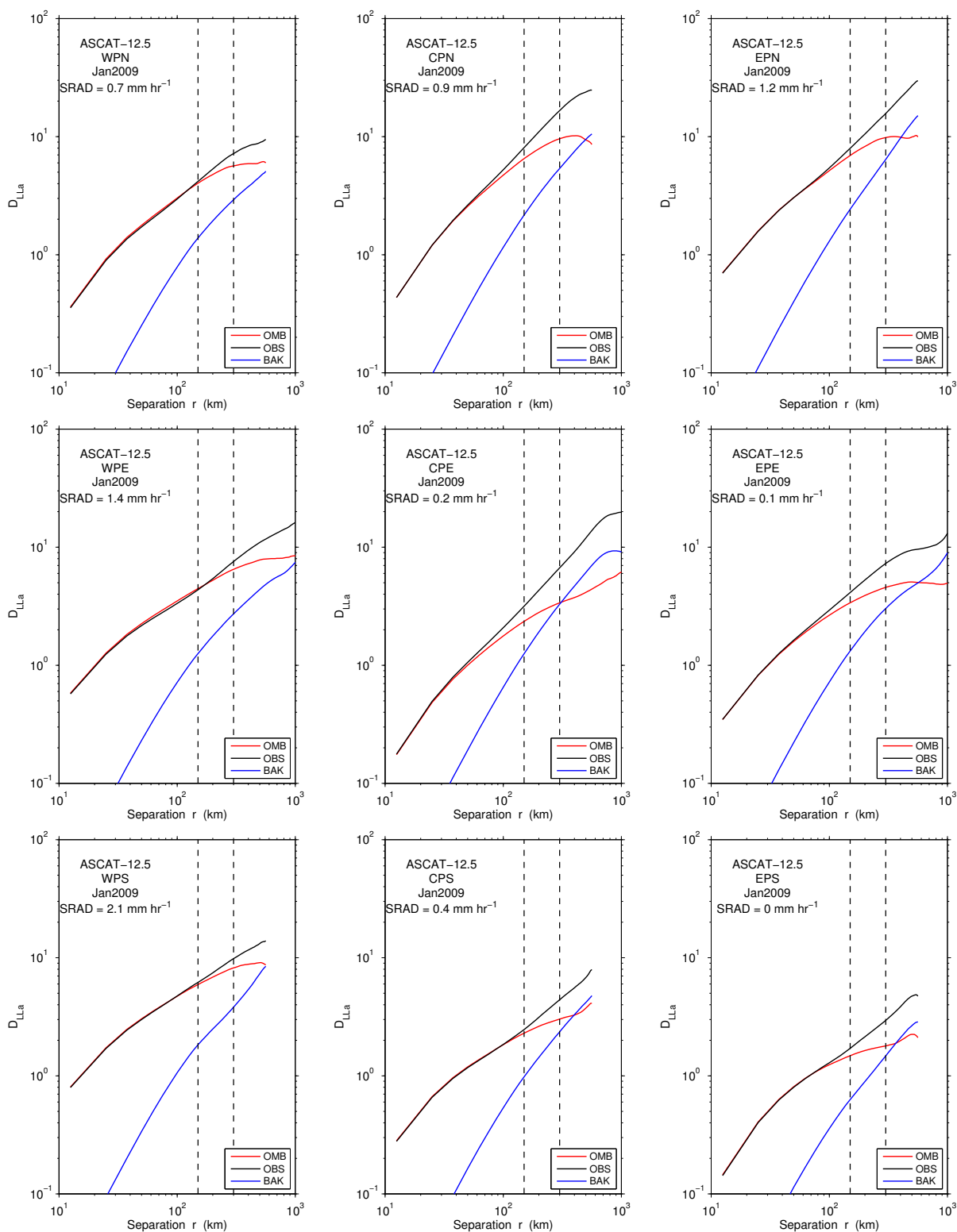


Fig. 20: D_{LL}^{omb} for ASCAT-12.5, January 2009

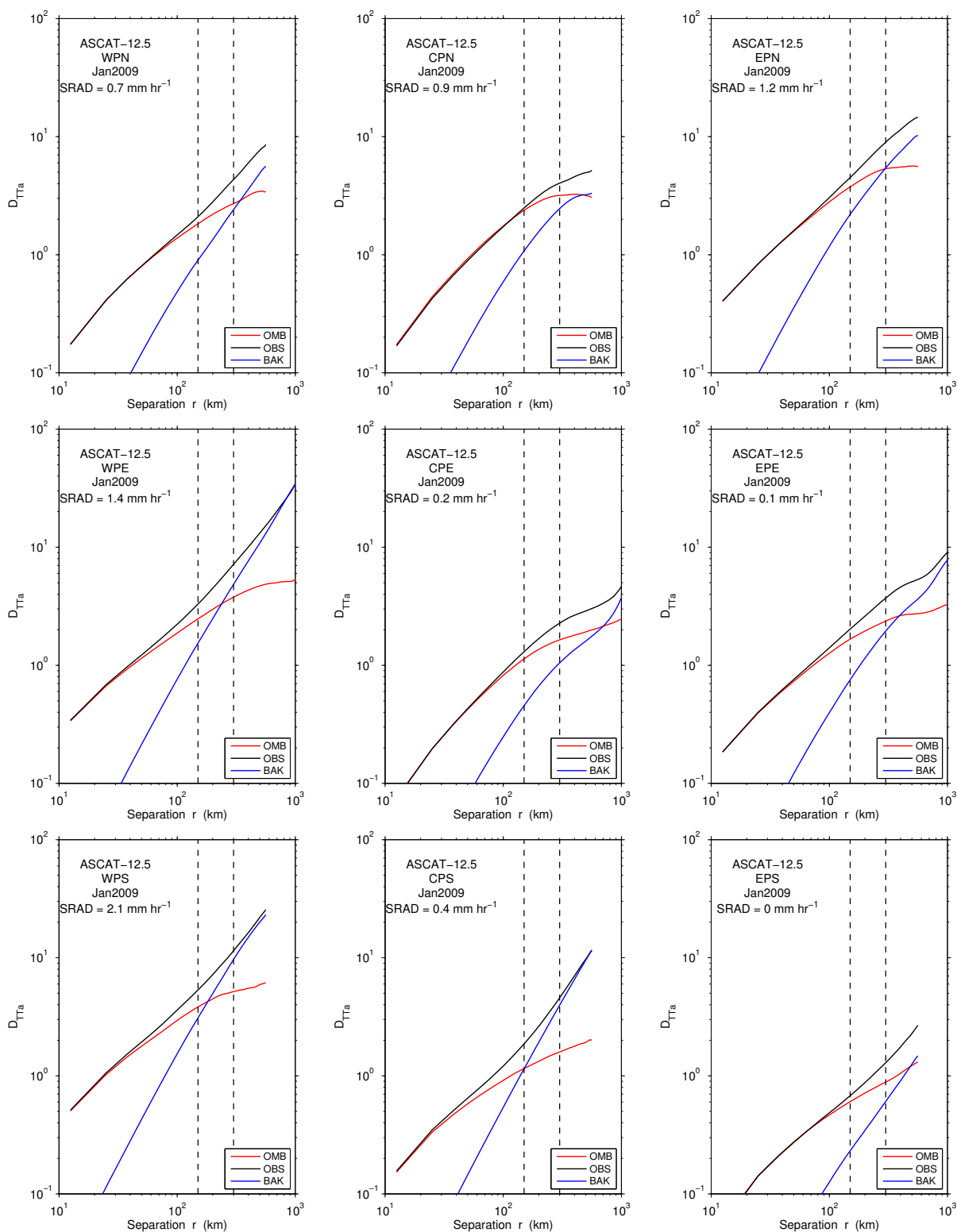


Fig. 21: D_{TT}^{omb} for ASCAT-12.5, January 2009

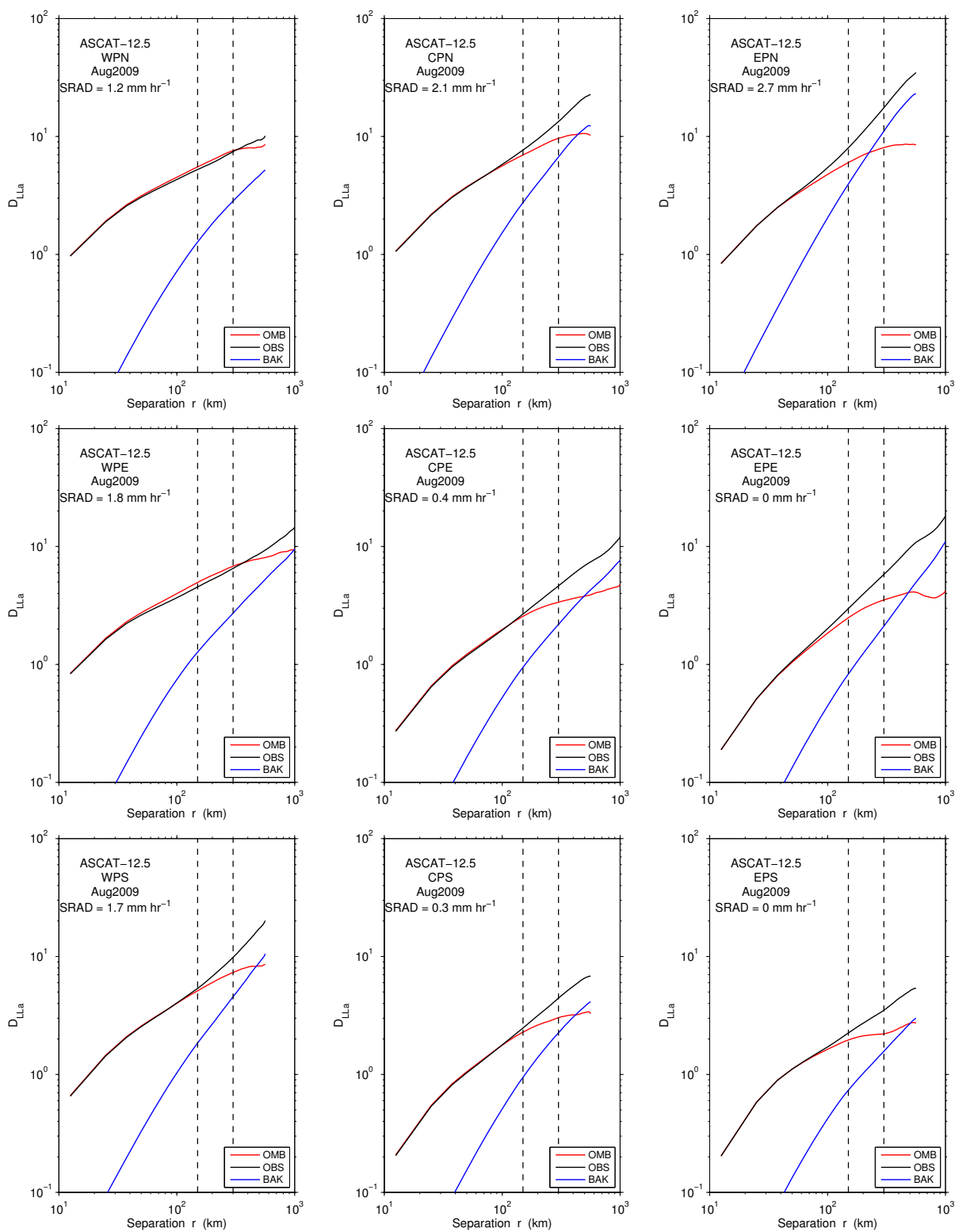


Fig. 22: D_{LL}^{omb} for ASCAT-12.5, August 2009

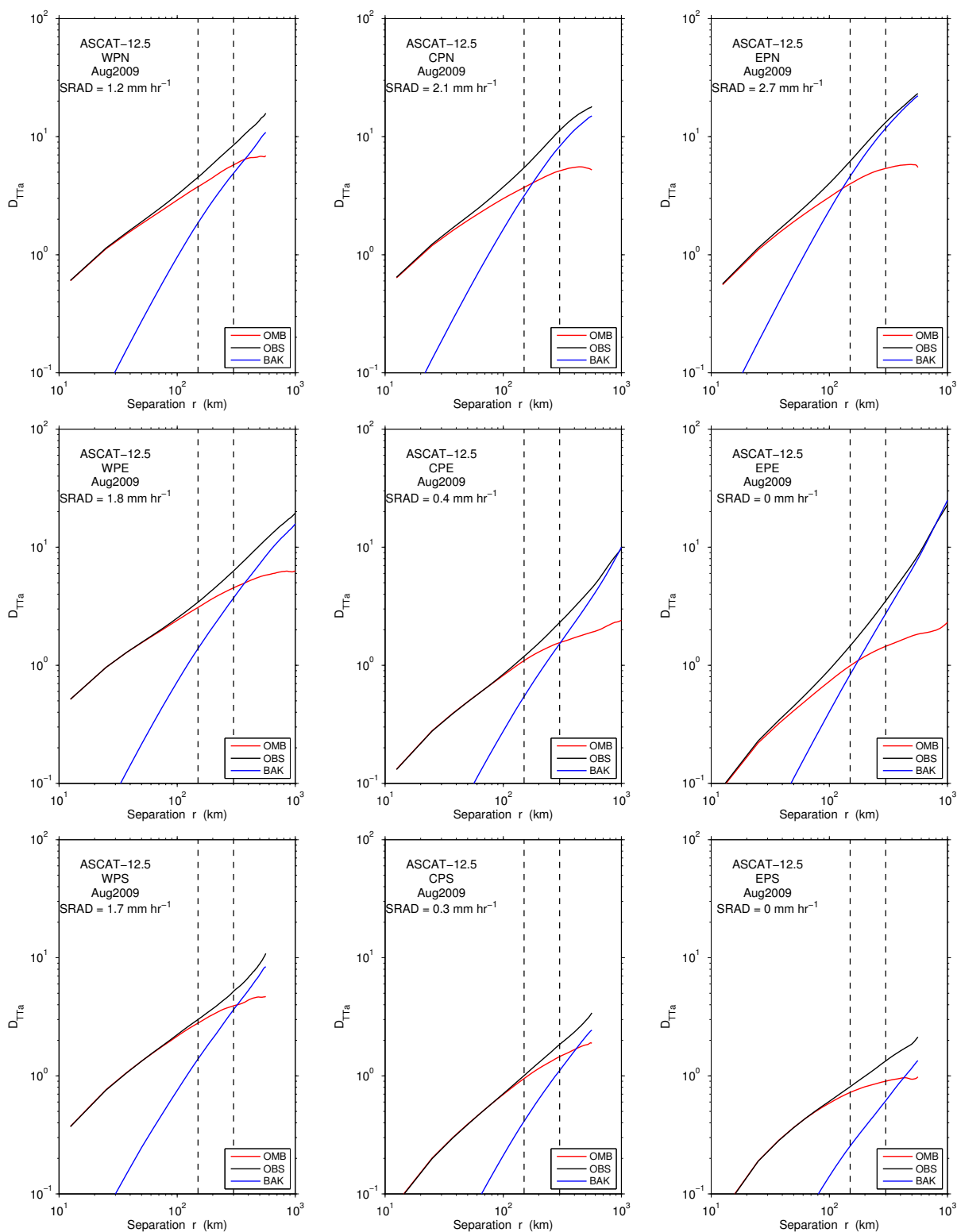


Fig. 23: D_{TT}^{omb} for ASCAT-12.5, August 2009

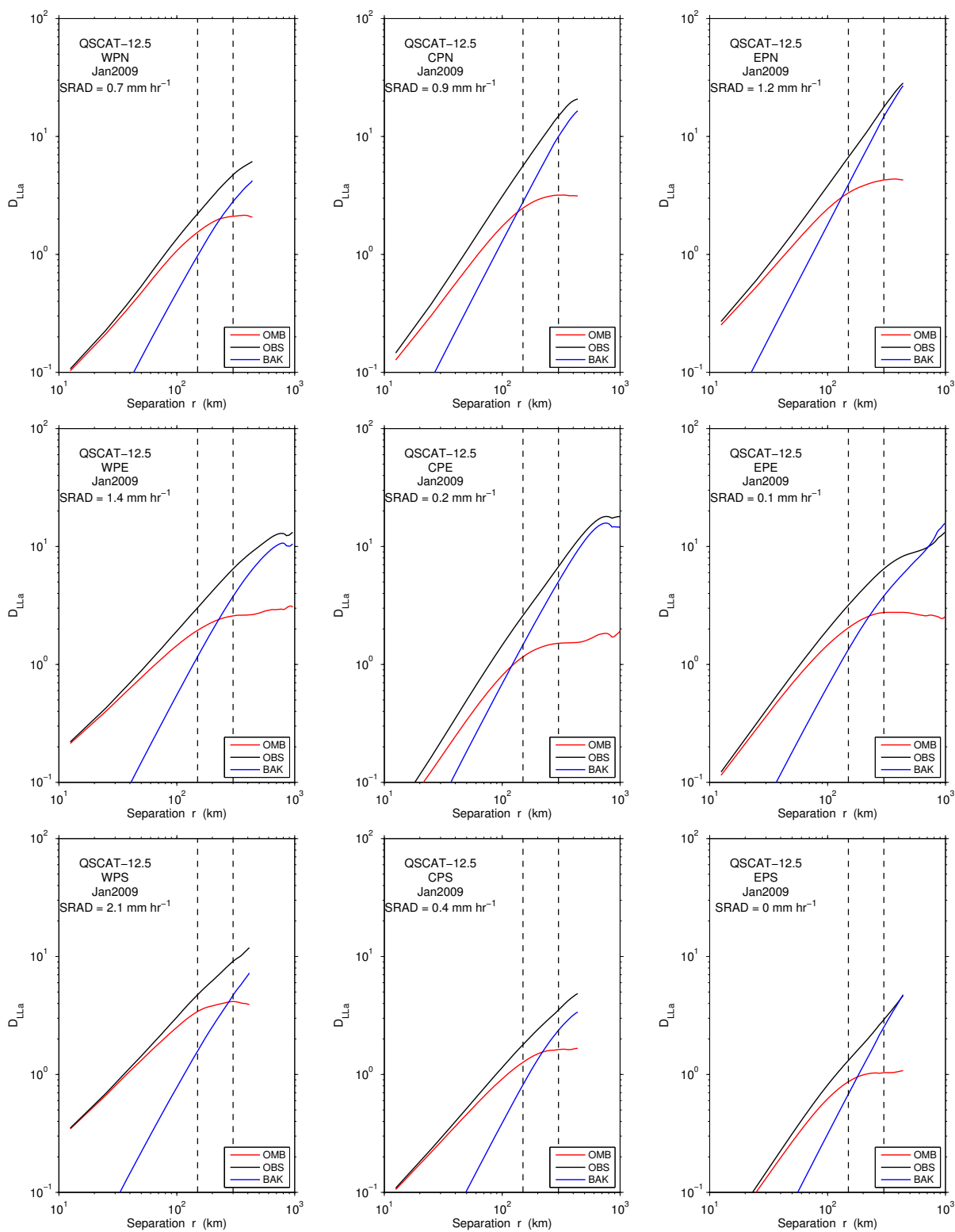


Fig. 24: D_{LL}^{omb} vs r for QSCAT-12.5, January 2009

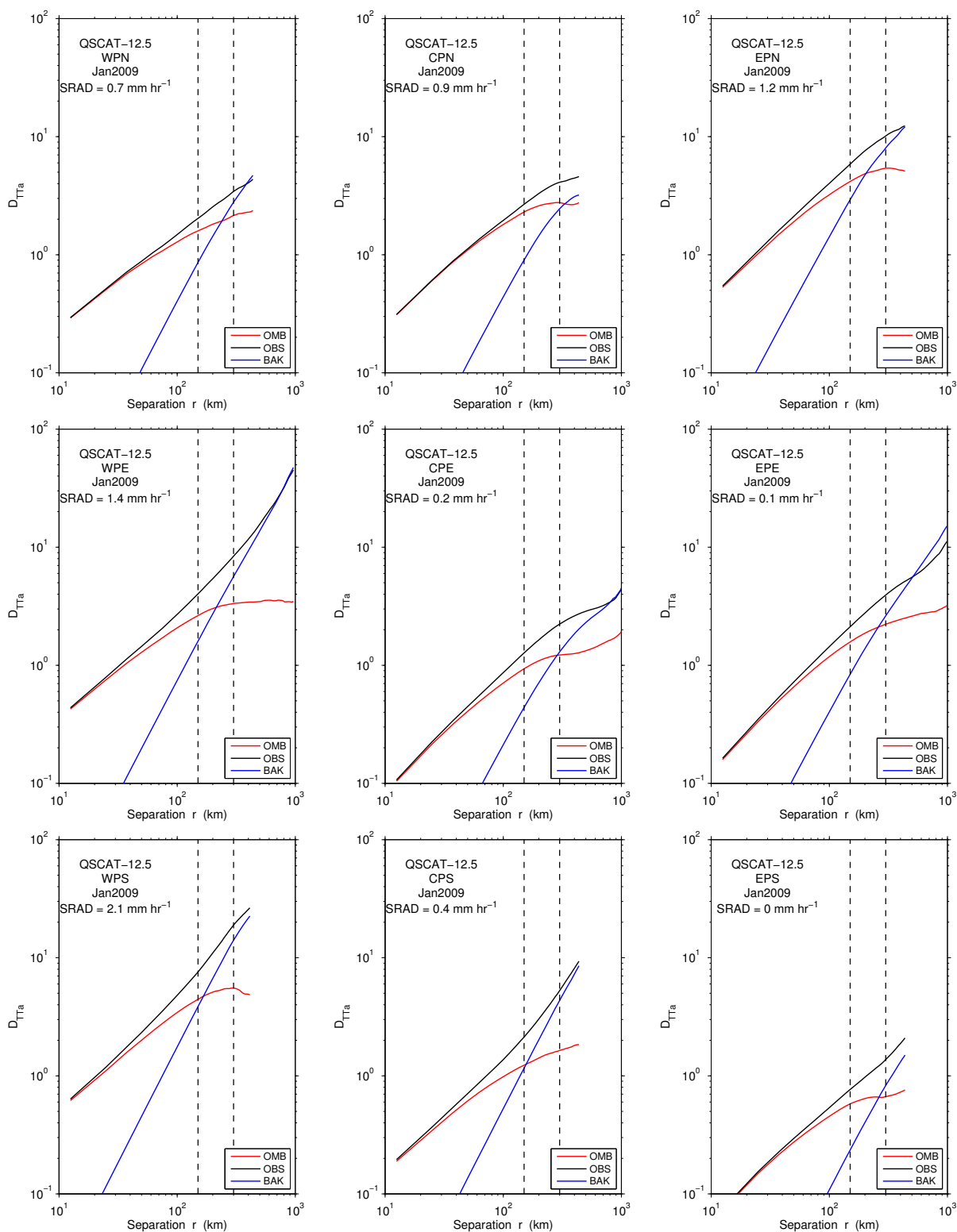


Fig. 25: D_{TT}^{oba} vs r for QSCAT-12.5, January 2009

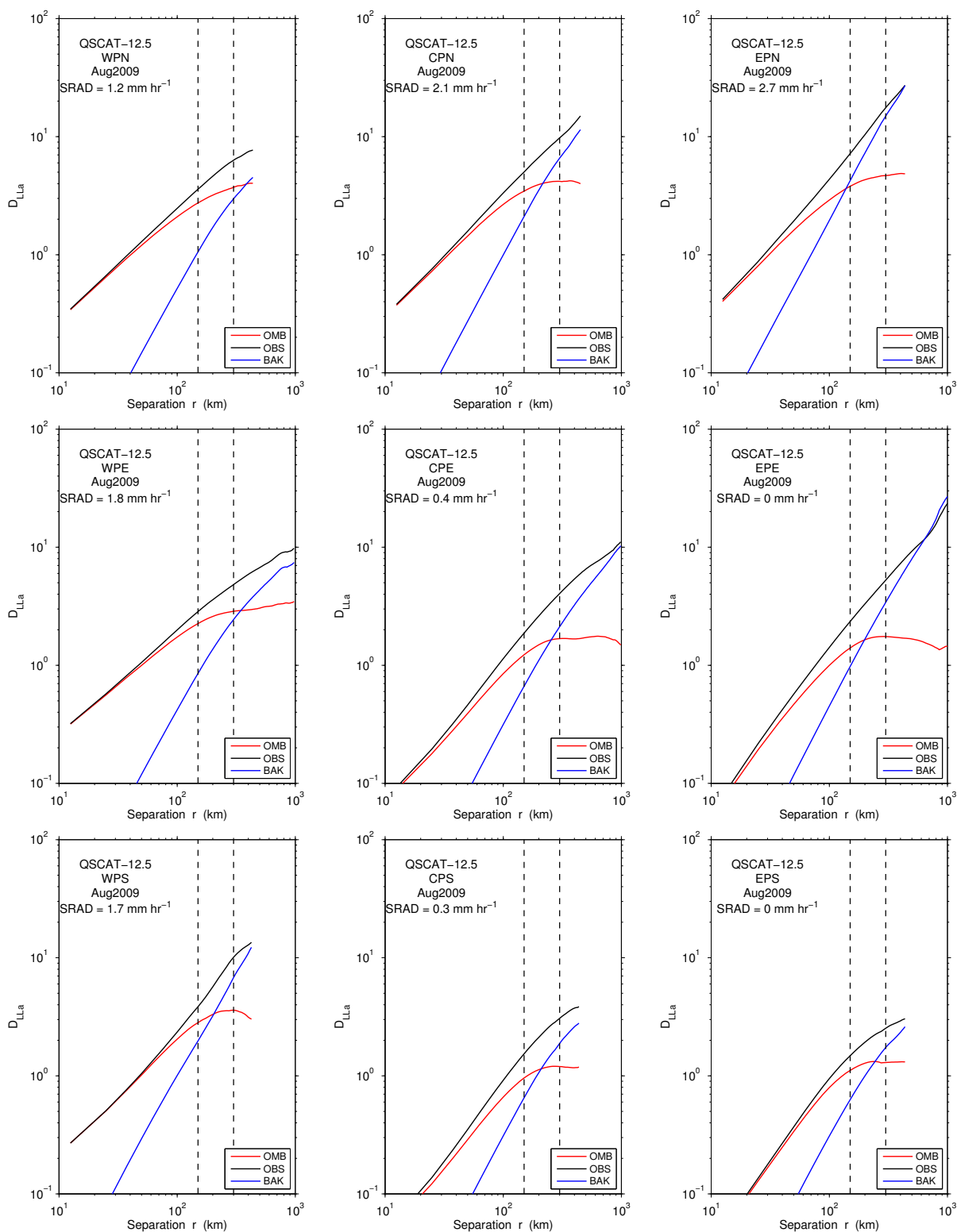


Fig. 26: D_{LL}^{omb} vs r for QSCAT-12.5, August 2009

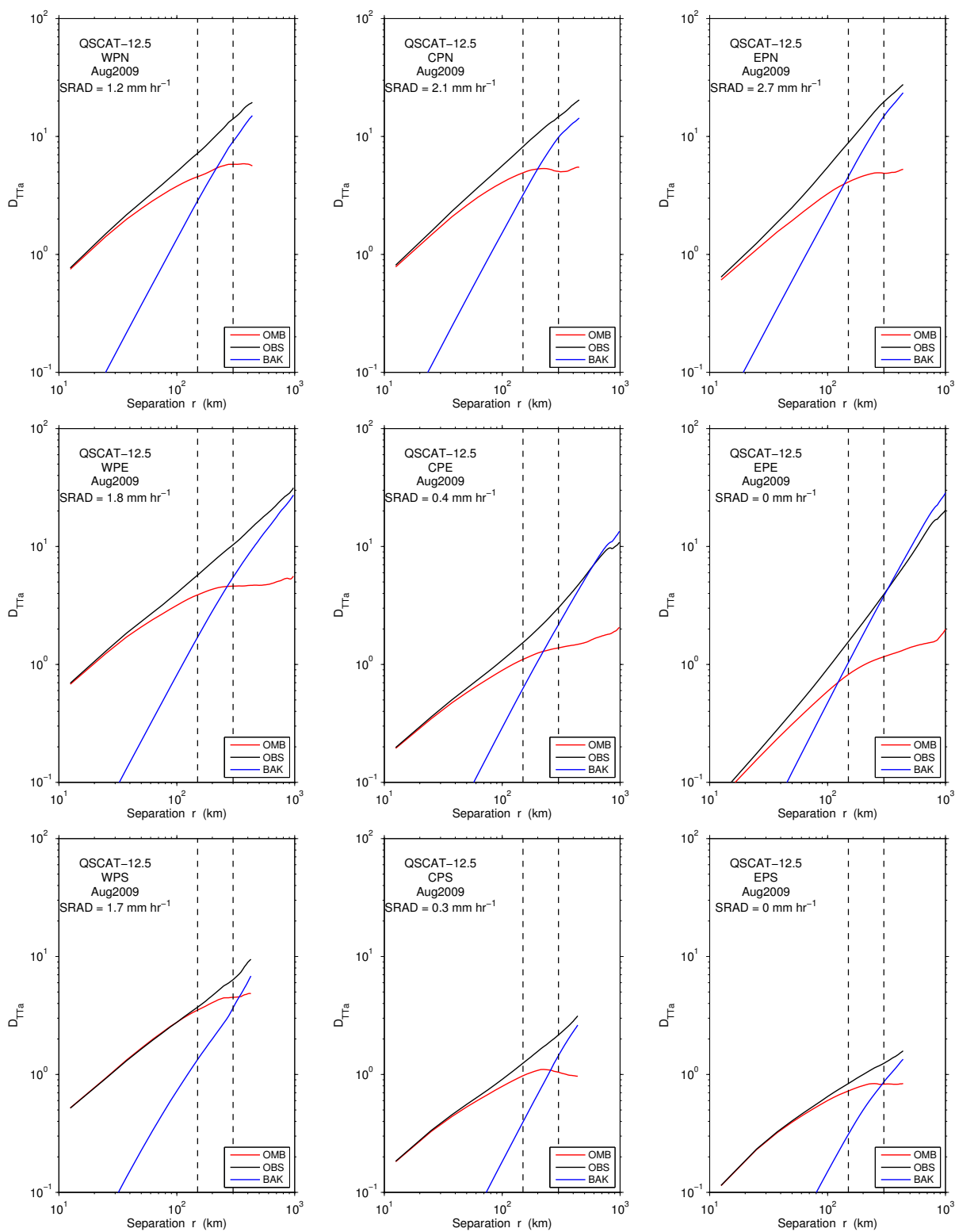


Fig. 27: D_{TT}^{omb} vs r for QSCAT-12.5, August 2009

10 Summary

In this paper, one-dimensional along-track structure functions were used to compare ocean vector winds derived from measurements by ASCAT-on-MetOp-A and SeaWinds-on-QuikSCAT. Monthly averaged structure functions were calculated for nine regions in the tropical Pacific for a 12-month period when both scatterometers were in operation (November 2008 – October 2009). Three quantities were extracted from the structure functions: (i) noise levels, estimated at $r = 0$ from fits to a symmetric and an asymmetric quadratic; (ii) structure function amplitudes at 300 km; and (iii) structure function slopes from fits in log-log space over the range 50 – 250 km.

Noise levels estimated from the symmetric quadratic (which forces zero derivative at $r = 0$) were always greater than zero and correlated well with rain-rate. SeaWinds noise levels were larger for the transverse component than the longitudinal component, while the opposite was true for ASCAT noise levels. This was consistent with previous work using triple collocation. Noise levels estimated from the asymmetric quadratic were strongly influenced by the spatial filtering used to reduce noise. Using the asymmetric fit: (i) SeaWinds-NOAA noise levels were positive (under-filtered) and correlated well with rain-rate; (ii) SeaWinds-KNMI and QSCAT-12.5 noise levels were always close to zero, and (iii) ASCAT-25 and ASCAT-12.5 were always negative (over-filtered).

Structure function amplitudes at 300 km were argued to be plausible proxies for the turbulent kinetic energy contained in scales less than 300 km. Amplitudes were low in dry regions (where winds were light) and higher in regions with strong convective and tropical cyclone activity. Amplitudes for the longitudinal component (K_{La}) were larger for ASCAT than SeaWinds products, while for the transverse component (K_{Ta}) ASCAT was nearly equal to SeaWinds in dry regions and in rainy regions in all except tropical cyclone seasons; then K_{Ta} was larger for SeaWinds than ASCAT.

The amplitude ratio K_{Ta}/K_{La} was argued to be a measure of the vorticity-to-divergence. ASCAT and SeaWinds ratios were in good agreement when $K_{Ta}/K_{La} < 1$. However, SeaWinds ratios were significantly larger than ASCAT ratios when $K_{Ta}/K_{La} > 1$ (most pronounced in the convectively active west Pacific). The median filter ambiguity removal method used in DIRTH essentially propagates wind direction continuity. This may be the cause of the enhanced vorticity-to-divergence found in the rainy regions and in rainy months in dry regions.

Structure function slopes β_L and β_T for different wind products increase and decrease together. However, slope magnitudes and their ratio are wind product dependent, reflecting differences in noise level and processing. Noise causes structure functions to flatten, while filtering causes them to steepen. SeaWinds-NOAA and QSCAT-12.5 both have larger noise in the transverse component, while ASCAT products have larger noise in the longitudinal component (Fig. 11). This is consistent with Fig. 19 which shows that $\beta_T/\beta_L < 1$ for SeaWinds-NOAA and QSCAT-12.5 and $\beta_T/\beta_L \gtrsim 1$ for ASCAT and SeaWinds-KNMI (except for SeaWinds-KNMI in the Central Pacific).

In a final section, structure functions for observations - background winds were presented for ASCAT-12.5 - ECMWF and QSCAT-12.5 - NCEP. Many of the OMB structure functions show some flattening near 300 km, implying that the background error correlation

goes to zero there, and hence that background errors affect only a limited area. This should be studied further to explore the possibility of using the OMB structure functions to estimate the background error correlation and using this information dynamically in 2DVAR.

References

- Babiano, A., C. Basdevant, and R. Sadourny (1985), Structure Functions and Dispersion Laws in Two-Dimensional Turbulence, *J. Atmos. Sci.*, *42*(9), 941–949, doi:10.1175/1520-0469(1985)042<0941:SFADLI>2.0.CO;2.
- Bourassa, M., et al. (2010), Remotely Sensed Winds and Wind Stresses for Marine Forecasting and Ocean Modeling, in *Proceedings of OceanObs09: Sustained Ocean Observations and Information for Society (Vol. 2)*, edited by J. Hall and D. Harrison, D.E. & Stammer, ESA Publication WPP-306, doi:10.5270/OceanObs09.cwp.08.
- Curran, P., and J. Dungan (1989), Estimation of signal-to-noise – A new procedure applied to AVIRIS data, *IEEE Trans. Geosci. Remote Sens.*, *27*(5), 620–628, doi:10.1109/TGRS.1989.35945.
- Davidson, P. A., and B. R. Pearson (2005), Identifying turbulent energy distributions in real, rather than Fourier, space, *Phys. Rev. Lett.*, *95*, 214,501, doi:10.1103/PhysRevLett.95.214501.
- Dewan, E. (1997), Saturated-cascade similitude theory of gravity wave spectra, *J. Geophys. Res. - Atmos.*, *102*, 29,799–29,817.
- Figa-Saldaña, J., J. Wilson, E. Attema, R. Gelsthorpe, M. Drinkwater, and A. Stoffelen (2002), The advanced scatterometer (ASCAT) on the meteorological operational (MetOp) platform: A follow on for the European wind scatterometers, *Can. J. Remote Sens.*, *28*, 404–412, doi:10.5589/m02-035.
- Fore, A., B. Stiles, A. Chau, B. Williams, R. S. Dunbar, and E. Rodriguez (2012), Point-wise Wind Retrieval and Ambiguity Removal Improvements for the QuikSCAT Climatological Data Set.
- Freilich, M. H., and D. B. Chelton (1986), Wavenumber spectra of Pacific winds measured by the Seasat scatterometer, *J. Phys. Oceanogr.*, *16*, 751–757.
- Hoffman, R. N., and S. M. Leidner (2005), An introduction to the near-real-time QuikSCAT data, *Wea. Forecasting*, *20*, 476–493, doi:10.1175/WAF841.1.
- Houze, R. A. (2004), Mesoscale convective systems, *Rev. Geophys.*, *42*, RG4003, doi:10.1029/2004RG000150.
- King, G. P., J. Vogelzang, and A. Stoffelen (2012), Second-order structure function analysis of scatterometer winds over the Tropical Pacific: Part 1. Spectra and Structure Functions, *Tech. rep.*, NWPSAF-KN-VS-008, EUMETSAT.
- KNMI (2011), *ASCAT Wind Product User Manual*.

- Lander, M. A. (1996), Specific Tropical Cyclone Track Types and Unusual Tropical Cyclone Motions Associated with a Reverse-Oriented Monsoon Trough in the Western North Pacific, *Wea. Forecasting*, *11*(2), 170–186, doi:10.1175/1520-0434(1996)011<0170:STCTTA>2.0.CO;2.
- Laupattarakasem, P., W. Jones, K. Ahmad, and S. Veleva (2005), Calibration/validation of the SeaWinds radiometer rain rate algorithm, in *OCEANS, 2005. Proceedings of MTS/IEEE*, vol. 3, pp. 2601–2604, doi:10.1109/OCEANS.2005.1640163.
- Lindborg, E. (1999), Can the atmospheric kinetic energy spectrum be explained by two-dimensional turbulence?, *J. Fluid Mech.*, *388*, 259–288.
- Lindborg, E. (2007), Horizontal Wavenumber Spectra of Vertical Vorticity and Horizontal Divergence in the Upper Troposphere and Lower Stratosphere, *J. Atmos. Sci.*, *64*(3), 1017–1025, doi:10.1175/JAS3864.1.
- Liu, W. T., and X. Xie (2002), Double intertropical convergence zones — a new look using scatterometer, *Geophys. Res. Lett.*, *29*, 2072, doi:10.1029/2002GL015431.
- Mahrt, L., and N. Gamage (1987), Observations of Turbulence in Stratified Flow, *J. Atmos. Sci.*, *44*(7), 1106–1121, doi:10.1175/1520-0469(1987)044<1106:OOTISF>2.0.CO;2.
- Masunaga, H., and T. S. L’Ecuyer (2010), The southeast Pacific warm band and double ITCZ, *J. Climate*, *23*, 1189–1208, doi:10.1175/2009JCLI3124.1.
- Mitchell, T. P., and J. M. Wallace (1992), The annual cycle in equatorial convection and sea surface temperature, *J. Climate*, *5*, 1140–1156.
- Patoux, J., and R. A. Brown (2001), Spectral analysis of QuikSCAT surface winds and two-dimensional turbulence, *J. Geophys. Res.*, *106* (D20), 23,995–24,005, doi:10.1029/2000JD000027.
- Pope, S. B. (2000), *Turbulent Flows*, Cambridge University Press.
- Portabella, M., and A. Stoffelen (2002), A comparison of KNMI Quality Control and JPL Rain Flag for SeaWinds, *Can. J. Remote Sens.*, *28*, 424–430.
- Portabella, M., and A. Stoffelen (2004), A probabilistic approach for SeaWinds data assimilation, *Quart. J. Royal Meteor. Soc.*, *130*, 127–159, doi:10.1256/qj.02.205.
- Portabella, M., A. Stoffelen, W. Lin, A. Turiel, A. Verhoef, J. Verspeek, and J. Ballabrera-Poy (2012), Rain effects on ASCAT retrieved winds: Towards an improved quality control, *IEEE Trans. Geosci. Remote Sens.*, *50*, 2495–2506, doi:10.1109/TGRS.2012.2185933.
- Stiles, B., B. Pollard, and R. Dunbar (2002), Direction interval retrieval with thresholded nudging: A method for improving the accuracy of QuikSCAT winds, *IEEE Trans. Geosci. Remote Sens.*, *40*, 79–89.
- Townsend, A. A. (1976), *The Structure of Turbulent Shear Flow*, 2nd ed., Cambridge University Press, Cambridge, England, pp. 6–16.

- Tsai, W.-T., M. Spencer, C. Wu, C. Winn, and K. Kellogg (2000), SeaWinds on QuikSCAT: sensor description and mission overview, in *Geoscience and Remote Sensing Symposium, 2000. Proceedings. IGARSS 2000. IEEE 2000 International*, vol. 3, pp. 1021–1023 vol.3, doi:10.1109/IGARSS.2000.858008.
- Vincent, E., M. Lengaigne, C. Menkes, N. Jourdain, P. Marchesiello, and G. Madec (2009), Interannual variability of the South Pacific Convergence Zone and implications for tropical cyclone genesis, *Climate Dyn.*, pp. 1–16, doi:http://dx.doi.org/10.1007/s00382-009-0716-3.
- Vogelzang, J., and A. Stoffelen (2012), NWP Model Error Structure Functions Obtained From Scatterometer Winds, *IEEE Transactions on Geoscience and Remote Sensing*, pp. 1–9, doi:10.1109/TGRS.2011.2168407.
- Vogelzang, J., A. Stoffelen, A. Verhoef, J. de Vries, and H. Bonekamp (2009), Validation of two-dimensional variational ambiguity removal on SeaWinds scatterometer data, *J. Atmos. Oceanic Technol.*, 26, 1229–1245, doi:10.1175/2008JTECHA1232.1.
- Vogelzang, J., A. Stoffelen, A. Verhoef, and J. Figa-Saldana (2011), On the quality of high-resolution scatterometer winds, *J. Geophys. Res.*, 116, C10,033, doi:10.1029/2010JC006640.
- Wikle, C. K., R. F. Milliff, and W. G. Large (1999), Surface wind variability on spatial scales from 1 to 1000 km observed during TOGA COARE, *J. Atmos. Sci.*, 56, 2222–2231.
- Wyrtki, K. (1989), Some thoughts about the west Pacific warm pool, in *Proceedings of the Western Pacific International Meeting and Workshop on TOGA COARE*, edited by J. Picaut, R. Lucas, and T. Delcroix, pp. 99–109, New Caledonia, ORSTUM, Centre de Nouma.
- Xie, S.-P., M. Ishiwatari, H. Hashizume, and K. Takeuchi (1998), Coupled ocean-atmospheric waves on the equatorial front, *Geophys. Res. Lett.*, 25, 3863–3866.
- Xu, Y., L.-L. Fu, and R. Tulloch (2011), The global characteristics of the wavenumber spectrum of ocean surface wind, *J. Phys. Oceanogr.*, 41, 1576–1582, doi:10.1175/JPO-D-11-059.1.
- Zhu, B., and B. Wang (1993), The 30–60-day convection seesaw between the Tropical Indian and Western Pacific Oceans, *J. Atmos. Sci.*, 50, 184–199, doi:10.1175/1520-0469(1993)050<0184:TDCSBT>2.0.CO;2.